Review

Pulsed laser ablation in liquid for micro-/nanostructure generation

Zijie Yan, Douglas B. Chrisey *

Department of Materials Science and Engineering, Rensselaer Polytechnic Institute, 110 8th Street, Troy, NY 12180, USA

A R T I C L E   I N F O

A B S T R A C T

Pulsed laser ablation in liquid is an approach for micro-/nanostructure generation directly from bulk materials. It has grown rapidly as a research field of photochemistry and physical chemistry in the last decade, and represents a combinatorial library of constituents and interactions, but the understanding of this library is still insufficient. This review attempts to build up a comprehensive mechanistic scenario of pulsed laser ablation in liquid and illustrate the underlying principles to micro-/nanostructure generation. Various structures produced by this method have been summarized that provide prototypes for potential applications in sensing, optoelectronics, and biomedicine, etc.
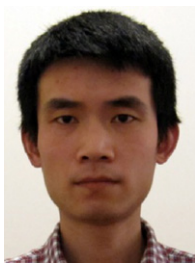
© 2012 Elsevier B.V. All rights reserved.

Contents

* Corresponding author. Tel.: +1 518 2763303; fax: +1 518 2768554.
  E-mail address: chrisd@rpi.edu (D.B. Chrisey).

Zijie Yan received dual BS degrees in Materials Science and Computer Science in 2005, and a MS degree in Physical Electronics in 2007, all from Huazhong University of Science and Technology (Wuhan, China). At Rensselaer Polytechnic Institute, he studied particle generation by pulsed excimer laser ablation in liquid under the direction of Prof. Douglas Chrisey, and obtained PhD degree in Materials Engineering in 2011. Currently he is a Postdoctoral Scholar in the James Franck Institute at the University of Chicago, applying optical forces to manipulate and control plasmonic nanostructures and chemical reactions.

Douglas B. Chrisey received a BS in Physics from State University of New York at Binghamton in 1983 and a PhD in Engineering Physics from the University of Virginia in 1987. He spent the next 17 years at the Naval Research Laboratory. Currently, he is a Professor of Materials Science and Biomedical Engineering at Rensselaer Polytechnic Institute. His research interests include the laser fabrication of thin films of advanced electronics, sensors, biomaterials, and materials for energy storage. The materials produced were used in device configurations for testing and typically have an improved figure-of-merit.

1. Introduction

A major challenge in nanotechnology is how to fabricate nanostructures with optimized figure-of-merit for different applications and from different materials. Generally, there are two classes of approaches to fabricate nanostructures, namely, bottom-up assembly and top-down fabrication [1]. Laser ablation of solids is a top-down method, which has attracted much interest ever since the invention of ruby laser in 1960s [2–5], because the high power density near the focus of a pulsed laser ($>10^6$ W/cm^2) allows this method to be applied to nearly all classes of materials. However, the generation of micro-/nanostructures by laser ablation is usually a bottom-up process represented by nucleation, growth and assembly of clusters from laser ablated species.

By definition, laser ablation is the ejection of macroscopic amounts of materials from the surface of a solid usually induced by the interaction of short ($\sim 10^{-13}$ to 10^{-8} s), intense ($\sim 10^6$ to 10^{14} W/cm^2) laser pulses with the surface. In principle, this can occur in vacuum, gas, and liquid, providing that the gas or liquid does not strongly attenuate laser energy and the light intensity (fluence) on the solid surface is still enough to perturb the material away from equilibrium state. The major application of laser ablation in vacuum or gas is the pulsed laser deposition (PLD) of thin films [6]. An important part of PLD's success came from the ability to deposit vapors in high pressures of reactive gases. Laser ablation in non-vacuum environments has benefits due to the reactions in a dense, but temporally short lived environment. It must be realized that bimolecular (biparticle) bonding in the gas phase requires a third body so as to conserve both momentum and energy. As such, the dense ablation plume near the target is a wealth of interesting particle bonding reactions. While laser ablation in gas has attracted considerable interest since the early 1980s, some researchers started to think about what would happen during laser ablation of solid targets in an even denser and more reactive medium – liquid.

Patil et al. are the pioneers to explore the synthesis possibilities at a liquid–solid interface by pulsed laser irradiation of iron in water in 1987 [7]. Later, Neddersen et al. reported the synthesis of colloids by laser ablation of metallic targets in water and organic solvents, and established this method as a simple yet reliable route to produce clean colloids without residual species [8]. The flourish of pulsed laser ablation in liquid (PLAL) for nanostructure generation started in the early 2000s, promoted by the synthesis and size control of noble metal nanoparticles (NPs) using laser ablation in aqueous solutions of surfactants [9].

This review primarily focuses on the fundamental mechanisms of PLAL and its recent applications to fabricate complex nanostructures other than solid nanospheres. There have been several reviews on PLAL for nanoparticle generation [10–16], but the understanding of its basic principles is still insufficient. Our review attempts to build up a comprehensive mechanistic scenario of PLAL and illustrate the combinatorial library of constituents and interactions. In the first section, we systematically analyze the ablation processes. Then we summarize the typical materials that have been investigated by PLAL, and discuss the unique aspects of fabricating complex nanostructures.

2. Fundamental mechanisms

2.1. Experimental setup and ablation process

Scheme 1(a) shows the schematic diagram of a typical experimental setup for PLAL. The setup basically only needs a pulsed laser, beam delivery optics, and a container to hold the target and liquid. The container as well as the target is usually rotating to avoid a deep ablation crater [10]. Alternatively, the laser beam can be delivered by scanner optics to move the ablation spot [17]. The setup may be modified to control the ablation process, but the common features still exist, that is, a laser beam is focused onto a target immersed in liquid, and the ablated materials are dispersed into the liquid.

PLAL represents a combinatorial library of constituents and interactions as illustrated in Scheme 1(b). The constituents of laser pulses, liquid media (including potential surfactant molecules/ions and electrolyte ions), solid targets and the ablated products may interact with each other. These interactions occur in the same system and in a short time after the laser pulse, thus are strongly coupled. The coupled interactions may lead to especially unique micro-/nanostructures that might not be envisioned by conventional fabrication techniques.

The ablation process has been studied by time-resolved shadowgraph technique using an intensified charge-coupled device camera synchronized with a flash lamp [18–20]. Fig. 1 shows a sequence of 10-ns-resolved shadowgraphs of a Nd:YAG laser (wavelength of 1064 nm, pulse duration of 8 ns) ablation of a Ag target in water [19]. Several unique phenomena could be identified: first, a shock wave was generated (Fig. 1c and d), followed by the formation of a cavitation bubble containing the ablation plume (Fig. 1e–g), and upon the final collapse of the bubble (Fig. 1h), the ablated materials were released into the liquid and a secondary shock wave was emitted (Fig. 1i). The mechanisms underlying these phenomena will be discussed in the following sections.

2.2. Laser penetration of the liquid

Within the common experimental setup of PLAL, the laser beam has to penetrate a liquid layer before reaching the solid surface. Two phenomena could happen during the process. First, the focal length of the focusing lens will change due to refraction or even self-focusing, typically for picoseconds (ps) and femtosecond (fs) lasers with high intensity, by the liquid layer [21,22]. Considering the refraction of a focused linear beam, the focal length will increase for

$$\Delta f = l \left(1 - \frac{f}{\sqrt{n^2 f^2 + (n^2 - 1)r^2}} \right), \tag{1}$$

where f is the focal length of the focusing lens in air, l is the liquid thickness, n is the refractive index of the liquid, and r is the radius
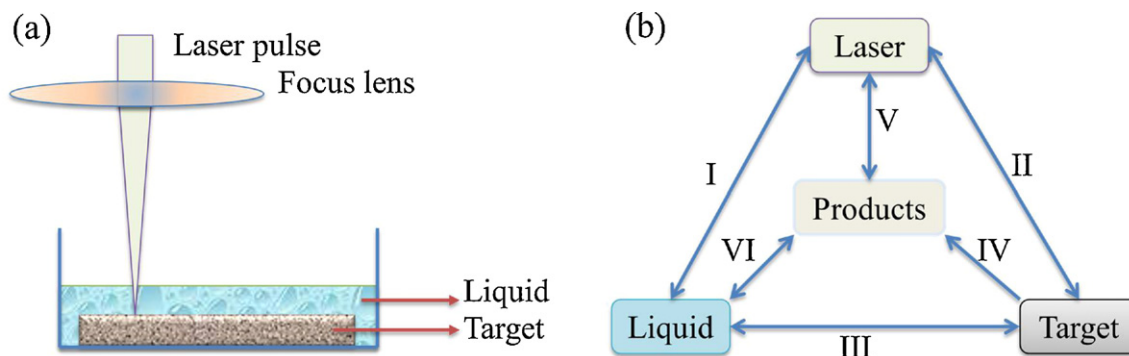
Scheme 1. (a) Schematic diagram of the experimental setup of PLAL. (b) A combinatorial library of constituents and interactions in PLAL: (I) laser–liquid interaction; (II) laser ablation of the target; (III) liquid–(hot) target interaction; (IV) generation of products from the target; (V) laser–products interaction; (VI) liquid–products interaction.
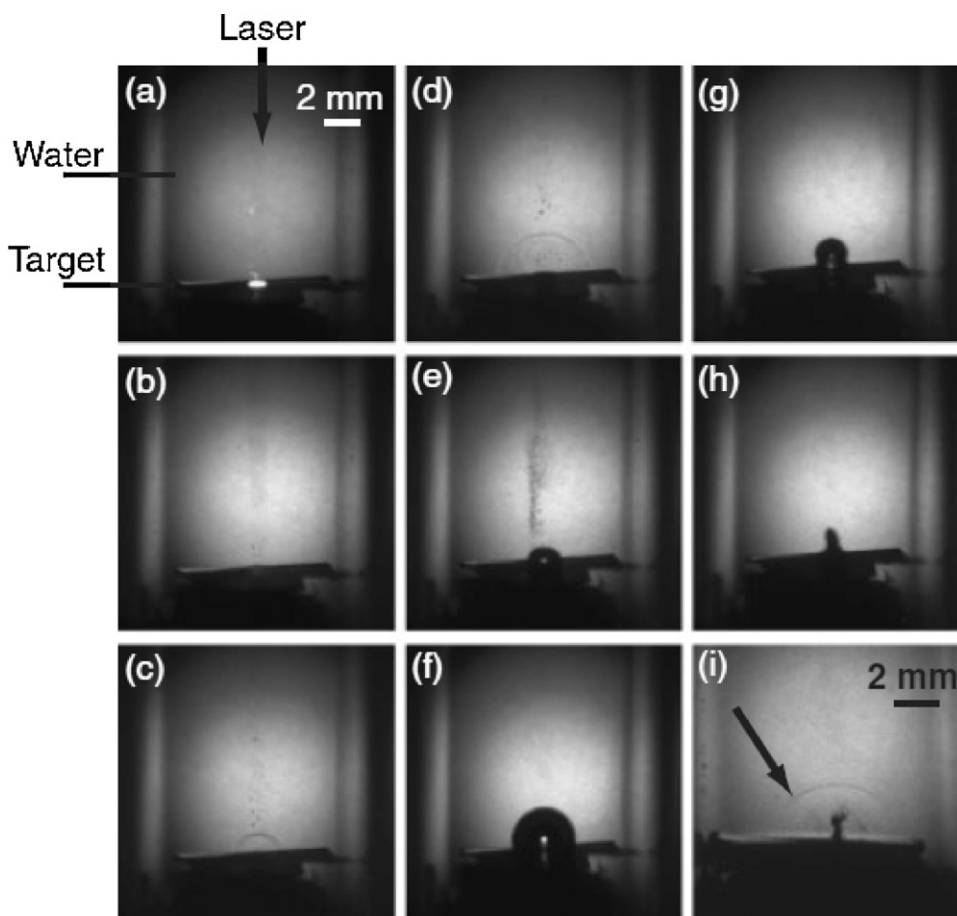

Fig. 1. Time-resolved shadowgraph images of a Nd:YAG laser (wavelength of 1064 nm, pulse duration of 8 ns) ablation of a silver target in water: (a) 0 ns, (b) 60 ns, (c) 570 ns, (d) 1.3 μs, (e) 9 μs, (f) 160 μs, (g) 260 μs, (h) 290 μs, and (i) 300 μs.
Source: Adapted with permission from [19].
© 2007 the Japan Society of Applied Physics.

of unfocused laser beam. For $r \ll f$, the formula can be simplified to

$$\Delta f = l\left(1 - \frac{1}{n}\right). \tag{2}$$

This is the length that the lens should be moved away from the solid surface to achieve optimum focusing. Strictly speaking, refraction of a laser beam that generally has a Gaussian profile is more complex; nevertheless, Menendez-Manjon et al. have applied the ABCD-transfer-matrix method to this problem and got the same result as Eq. (2) [21]. They have further analyzed other effects that

will also affect the focusing, such as the vaporization of the liquid at the liquid–air interface and the self-focusing phenomenon [21].

Second, the laser beam will be attenuated when it passes through the liquid. The attenuation is due to absorption of photons and to their scattering by liquid molecules. This can be caused by other matter in the liquid as well, such as surfactant molecules [23], ions, and particles produced by previous laser pulses. The light intensity decreases exponentially by

$$I_v = I_{v0} \exp[-\int_0^x \mu_v dx] \tag{3}$$

for a path length of x, where μ_v is the attention coefficient composed of the absorption coefficient α and the scattering coefficient at the light frequency v. In systems where absorption dominates, the attenuation can be expressed as the Lambert–Beer law

$$I_v = I_{v0} \exp(-\alpha x). \tag{4}$$

For an absorbing material, the optical penetration depth is related to the absorption coefficient by

$$\delta = \frac{1}{\alpha}. \tag{5}$$

Generally, the liquid in PLAL is assumed to be transparent, namely, δ is infinite. However, multiphoton absorption by liquid molecules may occur even at relatively low fluence [24], and this in turn, may cause photothermal heating and/or photodissociation of the liquid especially by lasers of short wavelengths (e.g., UV lasers). These effects could be enhanced by the overlapping of the reflected and incident laser beam. The jet-shaped shadow shown in Fig. 1a–c was assumed to form by the photothermal heating of water due to overlapped laser beam which changes the optical properties of water [19]. However, it may be also induced by the formation of bubble nuclei in the perturbed liquid molecules, which form macroscopic cavitation bubbles after the sweeping of the first shock wave (Fig. 1e). Such cavitation bubbles have been observed by Soliman et al. in the laser path after the first shock wave passed [20].

Attenuation by laser-produced particles will be more significant upon the increasing of ablation time which results in higher particle concentration [25], and especially for metallic nanoparticles, when the laser wavelength is in the excitation range of surface plasmon resonance of the nanoparticles [26]. Absorption of photo energies by laser-produced particles may cause secondary laser processing of the particles, such as heating/melting, welding/sintering, and fragmentation, and could be applied to fabricate unique nanostructures. The laser-induced heating/melting of powders in liquid was first applied to fabricate colloidal Cu particles by laser irradiation of CuO powders in 2-propanol [27,28]. Recently, this method regained interest as an approach to produce semiconductor and metal submicrometer spheres from irregular powers.[29–31]. Laser irradiation of CuO powders was further conducted in acetone very recently, which produced Cu nanoparticles or Cu_2O nanoparticles by rapid aerobic oxidation [32]. Laser ablation of HfS_3 powers in tert-butyl disulfide medium has shown the ability to synthesize Hf_2S nanoparticles with fullerene-like structures [33]. The laser-induced melting and vaporization could also cause size reduction or fragmentation of metal particles as a result of the ejection of atoms and/or small particles through vaporization of a heated particle [34].

Mafune et al. has employed laser-induced welding/sintering to solder Au and Pt nanoparticles by laser irradiation of a mixed solution [35], and the resulted Au@Pt network is shown in Fig. 2. They have also fabricated Au [36] and Pt [37] networks separately by first producing Au or Pt colloidal solution using PLA of an Au or Pt target in water, and then mixing the solution with sodium dodecyl sulfate (SDS) and irradiating it with a laser that could selectively heat the nanoparticles (e.g., the laser wavelength is close to the surface plasmon band of the metal particles).

For a laser with photon energy larger than the work function of a metal particle or even a half of that, the laser irradiation will also induce photoionization of the metal particle by a monophotonic or biphotonic process, which could cause fragmentation of the particle by spontaneous fission due to charge repulsion in the particle, namely, coulomb explosion [38,39]. The electron is considered to be ejected by thermionic emission via the excitation of the interband [40]. The fragmentation via coulomb explosion is fast and can occur in ~100 ps [39]. Other mechanisms have also been suggested based on laser-induced thermoelastic stress in the particle [41], or
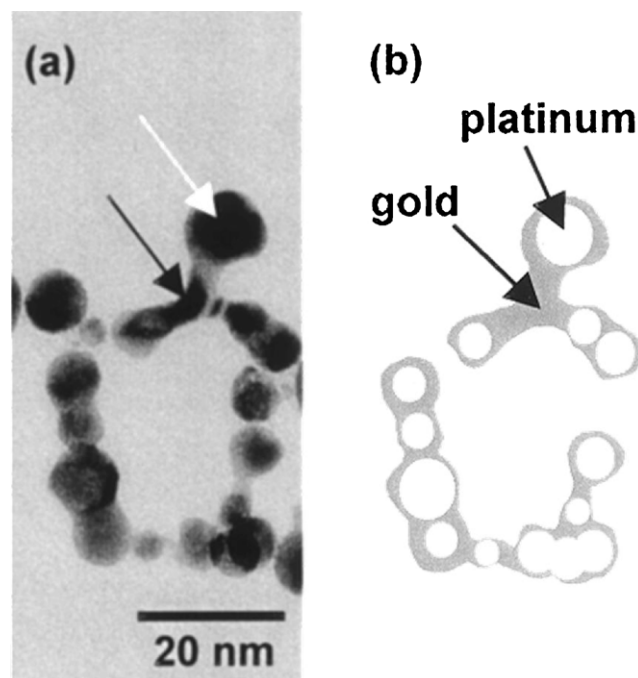

Fig. 2. (a) TEM image of Pt and Au nanowebs produced by laser irradiation at 532 nm onto a mixed solution of Pt and Au nanoparticles with a molar ratio of 0.2. (b) Schematic view of the nanoweb shown in panel (a).
Source: Adapted with permission from [35].
© 2003 American Chemical Society.

the collapse of bubbles formed on the laser-heated particle surface [12].

2.3. Shock wave emission

After passing through the liquid, the focused laser beam irradiates on the solid surface. The absorption of laser energy by the solid surface emits shock waves to relax the excess energy. By definition, a shock wave is the formation of discontinuities in flow variables, such as density [42]. Two distinct compressive waves are emitted and propagate into both the solid and liquid [43]. In the solid, rapid expansion immediately follows the shock wave. In the liquid, the shock front changes the refractive index, and thus the shock front can be observed by shadowgraph technique (e.g., a shock front became visible at ~50 ns in [19]). It can be also observed due to the deflections of a laser probe by the shock front [44]. Explosive collapsing of laser-induced bubbles will also emit shock waves, such as the one shown in Fig. 1i. The shock wave carries energy defined as the energy flux cross an area where a shock wave arrives [45]:

$$E_s = \frac{4\pi r_s^2}{\rho_l} \int_0^{t'} \frac{(P_s - P_l)^2}{U_s - ((P_s - P_l)/\rho_l U_s)} dt, \tag{6}$$

where r_s is the radial distance of the shock front from the origin, P is shock wave pressure, U_s is the shock front velocity, t' is the time at the tail of the shock wave while t is set as zero at the shock front.

Fig. 3a shows the propagation of the first shockwave emitted from PLA of Ag in water observed in Fig. 1. The velocity of the shock wave front was estimated to be ~2600 m/s before r_s = 0.5 mm, and ~1600 m/s in the later distance [19]. The latter value is comparable to the velocity of a shock wave generated by a τ_L = 30 ns laser focusing in liquid nitrogen, which was measured as 1675 m/s at r_s = 0.53 mm [45]. It is worth noting that the shock wave in the liquid nitrogen consumed ~35% of the laser energy of 36 mJ [45].

The shock wave in the liquid dissipates a considerable portion of the energy while it propagates. Across the shock wave the liquid
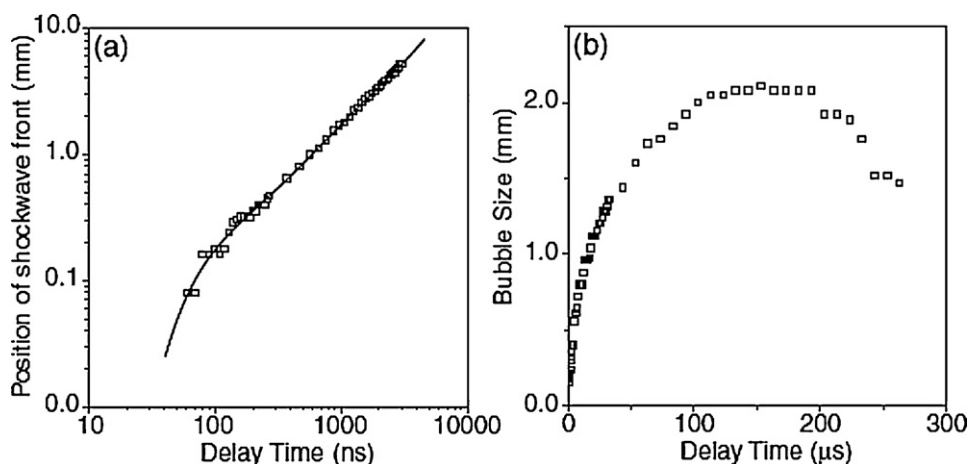
Fig. 3. Time profiles of (a) the propagation of the shockwave and (b) the growth and collapse of the cavitation bubble observed in Fig. 1.
Source: Adapted with permission from [19].
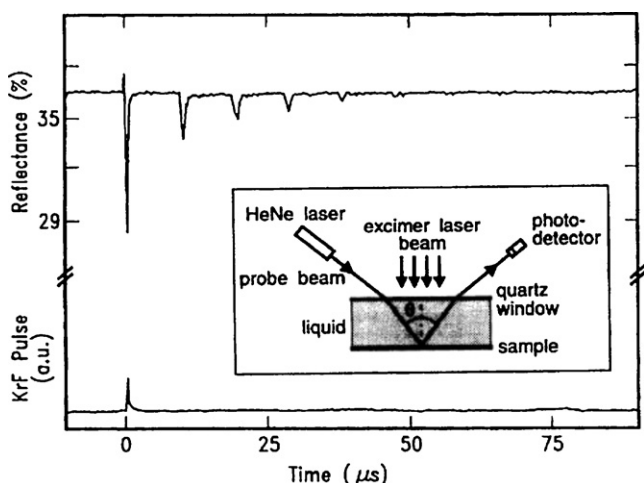© 2007 the Japan Society of Applied Physics.

Fig. 4. Optical reflectance signal due to bubble formation at a methanol–chromium interface [46]
© 1994 American Physical Society.

is heated. In particular, the shock wave may induce acoustic cavitation bubbles by travelling across the previously perturbed liquid by photothermal heating and/or photodissociation in the laser path. In previous studies using shadowgraph technique [19,20], the cavitation bubbles observed in the laser path at ~9 to 20 μs after the propagation of a shock wave were probably formed by this mechanism. Acoustic cavitation induced by shock wave has also been observed on a methanol-chromium interface using an optical reflectance probe [46]. Fig. 4 shows the optical reflectance signal due to bubble formation at the interface initially irradiated by an excimer laser pulse [46]. The laser irradiation induces microscopic bubbles in the heated liquid layer at the interface, and also leads to the generation of an acoustic pulse travelling between the chromium surface and the quartz window. The first reflectance drop is caused by the bubble formation due to laser heating of the chromium surface and the liquid layer above it, and the succeeding echoes are solely due to cavitation bubbles induced by the traveling shock wave [46].

2.4. Pulsed laser ablation of the solid

The deposition of photon energies on the target surface gives rise to hot carriers of electrons or electron–hole pairs at a temperature T_e. However, the pathways to ablation are varied depending on the pulse duration τ_L, fluence F, and the solid properties. At irradiances above a threshold I_p (~10^{13} W/cm² for metals and semi-conductors) [47], the laser pulse induces optical breakdown of the solid and a direct solid-to-plasma transition. Well below I_p, which is the case for most PLA experiments using nanosecond (ns) lasers and for some ps and fs lasers, both thermal and non-thermal channels may lead to ablation. Two characteristic time scales are worth mentioning first, namely, the electron–photon equilibration time τ_E (~10^{-12} to 10^{-11} s) [47,48] and liquid–vapor equilibration time τ_{LV} (~10^{-12} to 10^{-11} s according to [47] or ~10^{-9} to 10^{-8} s according to [49]). The non-thermal channel opens when a laser-induced structural modification occurs in a time $\tau_M < \tau_E$, while in most cases, $\tau_M \gg \tau_E$ and thermal pathways dominate [50].

In general, there are three kinds of thermal processes: (1) vaporization, (2) normal boiling, and (3) explosive boiling, which are determined by thermodynamic and kinetic limits [51]. Vaporization is the emission of atoms or molecules from the laser-irradiated surface by local perturbations. It has no temperature threshold but may be only important for $\tau_L \geq 100$ ns [51]. Normal boiling mainly occurs by heterogeneous nucleation, namely, a vapor bubble nucleates at the interface between superheated liquid with another phase, such as impurities and involved solids. By contrast, explosive boiling occurs by homogenous nucleation completely within a superheated liquid.

To illustrate the thermal processes, a typical *P*–*T* phase diagram for liquid–vapor transition is shown in Scheme 2. The binodal curve is the liquid–vapor equilibration curve described by Clausius–Clapeyron equation

$$\frac{dP}{dT} = \frac{L}{T\Delta V}, \tag{7}$$

where *L* is the latent heat and ΔV is the volume change of the phase transition. The intrinsic stability of a pure phase requires [52]

$$\left(\frac{\partial P}{\partial V}\right)_T < 0. \tag{8}$$

When the liquid is superheated beyond the binodal curve, it enters a metastable region, but the *stability criterion* (8) could be still satisfied until an upper limit. This limit is the spinodal curve where $\partial P/\partial V = 0$. Spontaneous nucleation can occur in the metastable region, the generation rate of bubbles at the critical size is given by [52]

$$J = \rho_{N,l} \left(\frac{3\sigma}{\pi m}\right)^{1/2} \exp\left\{\frac{-16\pi\sigma^3}{3k_B T_l [\eta P_{sat}(T_l) - P_l]^2}\right\}, \tag{9}$$
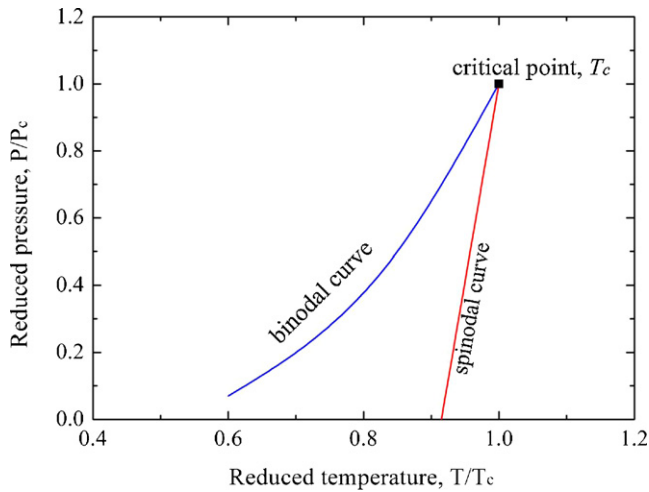
Scheme 2. Typical P–T phase diagram for liquid–vapor transition.

where $\rho_{N,l}$ is the number of liquid molecules or atoms per unit volume, σ is the surface tension, m is the mass of one molecule or atom, k_B is the Boltzmann constant, T_l is the liquid temperature, $P_{sat}(T_l)$ is the saturation vapor pressure at T_l, P_l is the ambient liquid pressure, and

$$\eta = \exp\left[\frac{P_l - P_{sat}(T_l)}{\rho_l R T_l}\right], \tag{10}$$

where ρ_l is the density of the liquid. According to Eq. (9), the spontaneous nucleation rate increases exponentially with T_l. And since it increases so rapidly, a narrow range of temperature exists that below the range spontaneous nucleation can be neglected and above the range it occurs immediately. The median temperature of this range, as named by *the kinetic limit of superheat* [52], is about 0.9 T_c [49]. Homogenous nucleation occurs at the kinetic limit of superheating, causing explosive boiling.

The explosive boiling, or *phase explosion* as a solid is rapidly heated at constant pressure, was suggested by Miotello and Kelly as the ablation mechanism for short laser pulses ($\tau_L \leq 1$ ms) [51,53]. Several experimental results support the phase explosion behavior of ns laser ablation [49,54]. However, numerical investigations by Lewis et al. show that phase explosion only occurs for ultrafast lasers of $\tau_L < \tau_{th} \sim 10^{-11}$ s (the characteristic time for heat conduction) [47,55]. In this range, the isochoric heating builds up a strong pressure, which is then released by mechanical expansion and pushes the material across the kinetic limit of superheat, and finally results in phase explosion [55]. For $\tau_L \geq \tau_{th}$, however, heating is slower and thermal diffusion is efficient. The expanding supercritical liquid follows the binodal curve and dissociates into liquid droplets/clusters under near-equilibrium condition [55], viz., a process called "trivial" fragmentation [56], and results in ablation. The "trivial" fragmentation directly produces liquid droplets that then form particles by cooling in liquid. Metallic particles formed by this way may form metal/metal oxide core/shell structures and even hollow particles by reaction with the liquid molecules. Recently, Liu et al. produced metal droplets by using a millisecond pulsed laser to ablate metal targets in liquid media, and the droplets from some metals could react with certain liquid molecules, resulting in hollow nanoparticles due to the nanoscale Kirkendall Effect [57,58].

The results of Lewis et al. indicate that the occurrence of phase explosion depends on the expansion dynamics of the target [47,55]. Expansion of the solid surface was not confined in the model, but this is not the case in the presence of a liquid layer. A numerical study by Perez et al. shows that the incompressibility of the liquid will confine the hot and pressurized material of the target

over long time scales and slow down its expansion [24]. Thus, even with ultrafast lasers, a liquid layer may sufficiently prohibit the occurrence of phase explosion, while ablation by vaporization and "trivial" fragmentation is more likely.

For a laser pulse of $\tau_L < 10^{-12}$ s, the plume will not absorb laser energy considering the liquid–vapor equilibration time $\tau_{LV} \geq 10^{-12}$ s [47,49]. However, for ns lasers typically with $\tau_L \sim 10^{-8}$ s, the ablation plume will absorb laser energy during the later stage of the laser pulses. The absorption is significant for ns ablation at relatively low irradiances, leading to maximum vaporization and ionization. Even at irradiances of 0.2–1.0 GW/cm^2 near the ablation threshold, a considerable part of the ablation plume could be ionized [59,60], namely, forming plasma. The plasma ionization can be calculated by the Saha equation [61]

$$\frac{n_{m+1}n_e}{n_m} = 2\frac{u_{m+1}}{u_m}\left(\frac{2\pi m_e k_B T}{h^2}\right)^{3/2}\exp\left(-\frac{I_{m+1}}{k_B T}\right) \tag{11}$$

for $m = 0, 1, \ldots$, where n_{m+1} is the number density of the $(m+1)$st ions (for neutrals it is $m = 0$), n_e is the number density of electrons, u_{m+1} is the partition function, m_e is the mass of electron, h is the Planck constant, and I_{m+1} is the $(m+1)$st ionization potential. It is worth noting the light field is generally not uniformly distributed over the area of the focal spot. In some local regions the irradiances may substantially exceed the average field and induce the first ionization [42]. The effect of plasma screening could result in the saturation of ablation rate under higher irradiances [49,61].

2.5. Laser-induced bubbles

A unique feature of PLAL is the generation of bubbles from the liquid layer at the solid–liquid interface. Two pathways can lead to the formation of bubbles in pure liquid. One is the explosive boiling when the liquid temperature is raised close to the *kinetic limit of superheat* by ΔT_c at roughly constant pressure. The other is often called cavitation when the liquid pressure falls below the tension strength of the liquid by ΔP_c at roughly constant liquid temperature. The interior pressure of a bubble with radius R is

$$P_B = P_\infty + \frac{2\sigma}{R}, \tag{12}$$

where P_∞ is the liquid pressure at infinity. Nucleation of cavitation occurs at the critical nucleation size R_c, and thus

$$\Delta P_c = \frac{2\sigma}{R_c}. \tag{13}$$

Generally, liquids, such as water, are not effective absorbing materials of laser. However, pulsed laser focusing in liquid could still induce bubbles by optical breakdown of the liquid when the irradiance is above a threshold I_p [62,63]. I_p depends on the laser wavelength. For example, I_p of water is $\sim 10^{13}$ W/cm^2 for a focused 1064 nm laser [63]; while for a focused 248 nm laser, I_p of water is just $\sim 2 \times 10^9$ W/cm^2 [64]. The expansion of plasma associated with the breakdown pushes the surrounding liquid, resulting in a cavitation bubble. With the existence of an absorbing solid surface, the situation is much different. Boiling of the liquid layer close to the heated surface almost inevitably takes place even at irradiance well below the ablation threshold of the solid. Study has shown that the bubble nucleation and explosive boiling occur at the surface of a Cr film heated by a 248 nm KrF excimer laser above a threshold of 1.7×10^6 W/cm^2 [65]. Physically speaking, cavitation and boiling have little different since ΔP_c and ΔT_c can be related by the Clausius–Clapeyron Eq. (7). We shall consider the two processes simultaneously, and refer them as *laser-induced bubbles*.

The nucleation of a bubble by PLAL may occur in the superheated liquid layer, but could also happen via heterogeneous nucleation at the solid–liquid interface. The bubbles in the foamy layer grow and
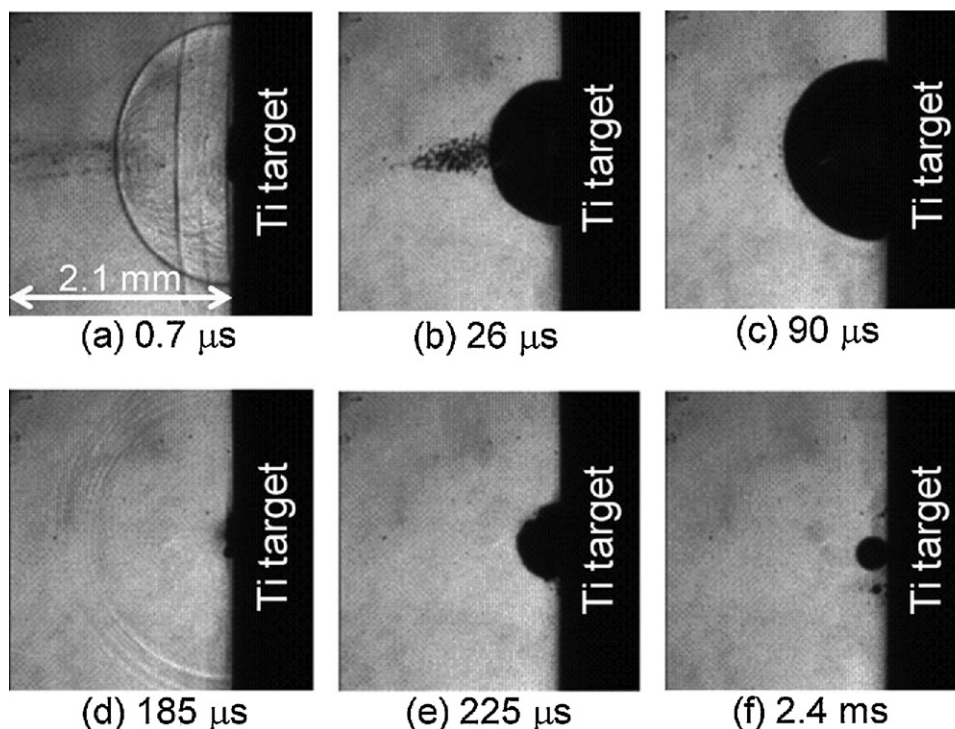
Fig. 5. Time-resolved shadowgraph images of cavitation bubbles produced by a Nd:YAG laser ablation of a Ti target in water [68].

aggregate into a single bubble along with the expansion of ablation plume. In macroscopic view by shadowgraph technique, only a nearly hemispherical bubble attached to the surface could be observed after $\sim 10^{-6}$ s as shown in Fig. 1e [19]. The bubble may detach from the surface by buoyancy and inertia forces from the liquid as it grows. We have observed such detached bubbles during PLAL by using co-linear camera [66]. The heterogeneous nucleation rate can be calculated by [52]

$$J = \frac{\rho_{N,l}^{2/3}(1+\cos\theta)}{2F}\left(\frac{3F\sigma}{\pi m}\right)^{1/2}\exp\left\{\frac{-16F\pi\sigma^3}{3k_BT_l[\eta P_{sat}(T_l)-P_l]^2}\right\}, \quad (14)$$

where θ is the liquid–solid contact angle, and

$$F = \frac{1}{2} + \frac{3}{4}\cos\theta - \frac{1}{4}\cos^3\theta. \quad (15)$$

For $\theta > 70°$, Eq. (14) gives a larger value than Eq. (9); while for $\theta < 65°$, Eq. (14) gives a smaller value [52]. Since the contact angle of water is typically 20° on a metal surface and 30–40° on an oxide surface [52], homogenous nucleation of bubbles should be dominant for most PLAL experiments.

For a spherical bubble growth, with the assumption that liquid is incompressible, the bubble boundary $R(t)$ can be described by the Rayleigh–Plesset equation [67]

$$R\frac{d^2R}{dt^2} + \frac{3}{2}\left(\frac{dR}{dt}\right)^2 = \frac{1}{\rho_l}\left(P_B - P_\infty - \frac{2\sigma}{R} - \frac{4\mu}{R}\frac{dR}{dt}\right), \quad (16)$$

where μ is the viscosity coefficient. Several effects are neglected in the equation, such as the stability of the bubble interface, the thermal effects, and the physical conditions within the bubble. Nevertheless, the equation can describe the oscillation behavior of bubble dynamics, that is, the bubble grows up to a maximum radius, and then collapses to a minimum size, and the cycle may repeat several times. Such oscillation behavior of a laser-induced bubble can be seen in Fig. 3b, which describes the profile of the bubble observed in Fig. 1. During the expansion, the pressure and temperature inside the bubble rapidly decrease; and during the collapse,

the pressure and temperature increase up to their original values. This may cause the expansion of a new bubble, and the emission of a secondary shock wave. The secondary shock wave and bubble can be observed in Fig. 5d and e, which shows the time-resolved shadowgraph images of a Nd:YAG laser ablation of a Ti target in water [68]. It is interesting that the secondary bubble finally evolved into a spherical bubble secondary bubble stationary in front of the target.

The energy of a spherical bubble is given by [45]

$$E_B \simeq \frac{4\pi}{3}R_{max}^3(P_\infty - P_B), \quad (17)$$

where R_{max} is the maximum size of the bubble. The bubble may oscillate several times, but because of the energy loss caused by the shock wave emission, heat conduction, and damping due to the liquid's viscosity, the R_{max} and oscillation time of the each cycle will decrease [68]. The explosive collapse can cause cavitation damage to the solid surface, which also induces material removal [69].

It has been shown that the bubble growth in a uniformly superheated liquid is initially inertia-controlled and $R(t) \propto t$. In the later stage, it is heat-transfer-controlled and $R(t) \propto t^{1/2}$. [52] The bubble growth near heated surface is more complex due to the lack of spherical symmetry and the nonuniformity of temperature field. However, it still shows stages of inertia and thermal effects [52]. The bubble on the laser ablated solid surface is in contact with the surface and nearly semispherical as shown in Figs. 1 and 5, partially depending on the liquid contact angle θ. The contact effect can be included in the Rayleigh–Plesset equation (16) by replacing σ with $\sigma\sin\theta$ [70].

In the absence of surface tension and gas content, Eq. (16) can be derived to give the time t_c required for completely collapse of bubble from $R = R_{max}$ to $R = 0$ [67]:

$$t_c \simeq 0.915\sqrt{\frac{\rho_l}{P_\infty - P_B}}R_{max}. \quad (18)$$

However, the bubble may contain gas contents such as hydrogen and oxygen. Several routes may generate atomic or molecular hydrogen and oxygen: the evolution of free radicals produced by

photodissociation [64] or collapsing of bubbles [71], the original soluble gas in the liquid [72], and the reaction byproducts of ablated materials with the liquid. When considering gas-filled bubbles in a unsaturated liquid, the collapse is determined by mass diffusion of the gas into the liquid, and the time t_{cs} for complete solution is [72]

$$t_{cs} \approx \frac{\rho_g R^2}{2D(c_s - c_\infty)}, \tag{19}$$

where ρ_g is the density of the gas in the bubbles, D is the diffusion coefficient of the gas in the liquid, c_s is the saturated concentration of the gas at the bubble interface and c_∞ is the ambient concentration.

The gas content can increase the stability of a laser-induced bubble. For example, considering water at 20 °C, $\rho = 998.2$ kg/m³, $P = 100$ kPa, $P_B = 2.33$ kPa, t_c calculated by Eq. (18) for a bubble with $R_m = 10$ μm is $\sim 9.3 \times 10^{-7}$ s. The typical value of $(c_s - c_\infty)/\rho_G$ is 0.01 [67], and D of gases in water at 20 °C are typically $\sim 2 \times 10^{-9}$ m²/s (e.g., $D_{hydrogen} = 4.25 \times 10^{-9}$ m²/s and $D_{oxygen} = 2.3 \times 10^{-9}$ m²/s [73], thus t_{cs} of a gas-filled bubble with $R_m = 10$ μm is ~ 2.5 s. That is a 6 order of magnitude increase of the bubble's collapse time. The gas-containing bubbles may also collapse into metastable ultramicroscopic bubbles, which could serve as long-lived cavitation nuclei [46].

Another factor that affects the he bubble's lifetime is the viscosity of the liquid. Increasing viscosity will decrease the rates of bubble growth and collapse, the bubble oscillation undergoes less damping in the liquid and thus has longer lifetime [74,75].

The lifetime of a bubble can be also increased by adsorption of impurities, such as nanoparticles, to the bubble interface that sterically hinder the interface movement [72]. Similar effect has been intensively studied in the research area of foam formation [76,77].

2.6. Nanocluster formation

The expansion or collapse time of a laser-induced bubble in its first oscillation cycle is generally 100–200 μs [19,20,63]. During the expansion, the ablation plume rapidly cools down. Electrons and ions recombine primarily by three-body collisions with an electron as the third body [42], and condensation will occur in the vapor. The condensation proceeds in two stages, namely, nucleation of critical clusters and growth of the nuclei. The dynamic condensation of expanding vapor has been described by the Zel'dovich–Raizer theory [42]. The plume expansion obeys the equation

$$\left(\frac{R}{R_0}\right)^2 = 1 + 2\frac{u_0}{R_0}t + \left[\left(\frac{u_0}{R_0}\right)^2 + \frac{16}{3}\frac{E}{MR_0^2}\right]t^2. \tag{20}$$

Comparison of Eqs. (16) and (20) indicates that the expansion profiles of laser-induced bubble and ablation plume are different, and thus the confinement on the plume is inhomogeneous. The energy barrier to form a spherical condensed cluster is

$$\Delta G = -\frac{4}{3}\pi r^3 \rho_N \Delta \mu + 4\pi r^2 \sigma, \tag{21}$$

where ρ_N is the number density of atoms in the cluster, $\Delta\mu$ is the chemical potential change between a condensed and uncondensed atom. The critical size of homogeneous nucleation can be calculated from $d(\Delta G)/dr = 0$, and

$$r_c = \frac{2\sigma}{n\Delta\mu}. \tag{22}$$

However, study has shown that the ions in the ablation plume could depress the energy barrier of clustering due to dielectric attraction to surrounding vapor atoms, which increases the nucleation rate, and consequently, decreases the average cluster size [78].

The nucleation rate changes extremely rapidly with the supercooling [79,80]

$$\frac{dv}{dt} \propto \exp\left(-\frac{16\pi\sigma^3 m^2}{3k_B^3 q\rho_l}\frac{T_{eq}^2}{T_v(T_{eq} - T_v)^2}\right), \tag{23}$$

where T_{eq} is the equilibrium temperature along the binodal curve, q is the heat of evaporation. Both of r_c and the nucleation rate depend on the vapor temperature T_v, which is determined by two competitive effects: the cooling due to plume expansion and the heating by vapor condensation [81]. In vacuum and gas, the condensation will eventually stop due to the high cluster temperature and low vapor pressure [78,81].

Condensation of plume in liquid will be much different from that in vacuum and gas. Due to the finite lifetime and oscillation behavior of the bubble, nanocluster formation will strongly rely on the nucleation time. The nucleation time scale of ablation plume in gas has been investigated by time-resolved photoluminescence (PL), Rayleigh scattering (SC) technique and re-decomposition laser-induced fluorescence (ReD-LIF) [82–84]. By using PL and SC, the onset times of nanocluster formation were measured to be 150–200 μs by PLA of Si in 10 Torr He, and 3 ms by PLA of Si in 1 Torr Ar [84]. The results from ReD-LIF show that clustering started at ∼200, 250, 300, and 800 μs by PLA of Si in 10 Torr He, Ne, Ar, and N₂, respectively [82,83]. If we consider the similar onset time of clustering in He and assume these all of the times reflect the true nucleation times, then increasing the pressure of Ar from 1 to 10 Torr will decrease the nucleation time from 3 to 0.3 ms. In other words, increasing the confinement of the ablation plume will decrease the nucleation time, although it also depends on the type of buffer gas. The pressure of PLAL experiments generally is the normal atmosphere (760 Torr), and the liquid layer exerts a strong inertia confinement, thus the nucleation time may be in the order of 10^{-5} s or shorter, depending on the liquid type and solid properties, etc. A typical time is very likely larger than the isothermal nucleation time of 10^{-10}–10^{-9} s calculated by Wang et al. [85]. Nevertheless, it should be still smaller than the time of first oscillation of a laser-induced bubble ($\sim 10^{-4}$ s), and thus it is expected that clustering and growth of the clusters, namely, formation of nano- or even micro-particles occurs in the laser-induced bubble. The change of bubble's lifetime and rates of growth and collapse will affect the interior condition, which in turn, exerts influence on the nanocluster formation. One instance is that when we ablated Ag in water using a pulsed excimer laser, only weakly oxidized Ag nanoparticles with sizes less than 100 nm could be observed. But when we added polysorbate 80, Triton X-100, or PVP into the water, which increased the viscosity of the liquid and thus the lifetime of the bubble containing the ablation plume, larger Ag particles with sizes up to micrometers could be produced [23].

During the bubble oscillation, the matter in the plume fringe may accumulate on the bubble interface similar to the situation of PLA in gas [86]. This effect will be more significant during the collapse of the bubble, when the momenta of the plume fringe and bubble interface are in inverse directions. Some of the accumulated matter, especially electrons and ions, may dissolve into the liquid and form a solution, thus nanocluster nucleation and/or chemical reactions could occur in the nearby liquid. During a rapid collapse, the bubble produces an intense local heating again. The hot spot could have temperature of ∼5000 K and pressure of ∼10⁸ Pa with heating and cooling rates of >10¹⁰ K/s [71]. In the hot spot, the clusters may form metastable phase, or be transformed into vapor again. Generally the bubble oscillates no more than two cycles [19,20]. The final collapse will release the interior matter, namely, vapor, clusters, and/or micro-/nanoparticles into the liquid. The micro-/nanoparticles may also form by cooling down of unionized

liquid droplets produced by "trivial" fragmentation of the target surface, which will broaden the size distribution of the products.

2.7. Chemical reactions

The liquid medium in PLAL not only confines the laser-induced plasma and serves as a reservoir of the laser-ablated species, but may also provide a reactive environment to generate compound from a target with single element. The laser-produced ions, atoms, clusters, and particles may react with the liquid molecules, surfactant molecules/ions, and electrolyte ions in the liquid. Typical examples are the formation of Zn/ZnO particles by PLA of Zn in water [87], the fabrication of nanocomposite of β-Zn(OH)$_2$ and zinc dodecyl sulfate by PLA of Zn in aqueous solutions of SDS [88], and the synthesis of AgCl by PLA of Ag in aqueous solutions of NaCl [89]. Yang suggested that the reactions could also occur in the laser-induced plasma or at the interface of the plasma containing excited/ionized species from the liquid [11], but we think that the reactions in the liquid should dominate considering that some of the products, such as Zn(OH)$_2$ and AgCl, are easy to decompose and could hardly exist in the hot plasma.

Surface oxidization is common for metallic nanoparticles produced by PLAL, including nanoparticles of noble metals [90–93]. Sylvestre et al. found that the Au nanoparticles produced by femtosecond laser ablation of Au target in distilled water were negatively charged, and proposed it was due to partial oxidation of the Au nanoparticle surface. Hydroxylation of the Au–O compound generates Au–OH, which then gives surface Au–O$^-$ by a proton loss resulting in the negative charging [90]. Further study by Muto et al. shows Au nanoparticles produced by nanosecond laser ablation in liquid were also negatively charged, and the partial oxidization of surface atoms was confirmed [91]. The surface charging not only makes the nanoparticles extremely stable in the colloidal solution [94], but also provides the possibility for functionalization of their surface by specific interactions [90]. Messina et al. have taken advantage of these properties to study the plasmon-enhanced optical trapping of gold nanoaggregates [95]. They first fabricated stable Au colloidal solution by pulsed laser of Au target in water, and then triggered and controlled aggregation of the Au nanoparticles by adding pyridine into the solution and finally used bovine serum albumin to stabilize the nanoaggregates. This method has shown largely increased trapping efficiency due to the strong field-enhancement driven by the nanoaggregates [95].

Very recently, Liu et al. developed a simple and catalyst-free route to fabricate polyoxometalate nanostructures by electrochemistry-assisted PLAL [96]. They used pulsed laser to ablate one metallic target in liquid and used another metal as the electrodes of an electrolytic cell combined with the PLAL system, and compounds containing both the species could be obtained from the liquid. A schematic illustration of this method is shown in Fig. 6A. Fig. 6B and C shows the images of Cu$_3$(OH)$_2$(MoO$_4$)$_2$ nanorods fabricated by using Mo as the target of PLAL and Cu as the electrodes in the electrolytic cell. Well-defined Cu$_3$Mo$_2$O$_9$ nanorods have been obtained by further annealing the Cu$_3$(OH)$_2$(MoO$_4$)$_2$ nanostructures at 500 °C [96].

3. PLAL for micro-/nanostructure fabrication

3.1. PLAL of various target materials

A large variety of target materials, including metals, alloys, semiconductors, and ceramics, have been used and investigated for nanostructure generation by this technique. Some typical works are summarized in Table 1.
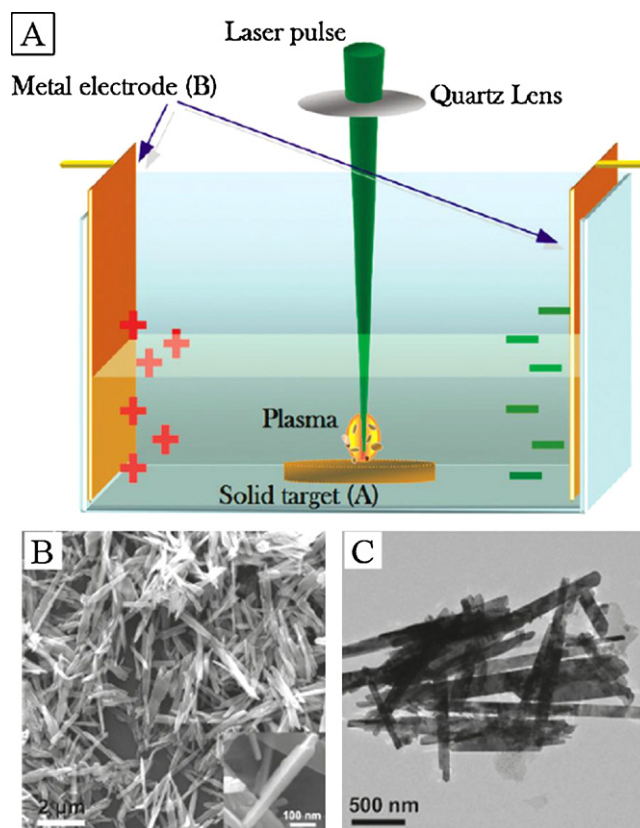
Fig. 6. (A) Schematic illustration of electrochemistry-assisted laser ablation in liquid. (B) scanning electron microscopy (SEM) and (C) transmission electron microscopy (TEM) images of Cu$_3$(OH)$_2$(MoO$_4$)$_2$ nanorods fabricated by using Mo as the solid target and Cu as the electrodes.
Source: Adapted with permission from [96].
© 2011 American Chemical Society.

It can be seen from Table 1 that PLAL has the ability to produce micro-/nanostructures from a large variety of targets. It is worthy noting that PLAL can be also applied to fabricate organic nanoparticles, such as oxo(phtalocyaninato)vanadium(IV) [181] and quinacridone [182] nanoparticles reported by Asahi and co-workers.

Among the various parameters of the experimental conditions, the liquid medium could play important roles on most of the phenomena described in Sections 2.2–2.7. Secondary laser processing of the fabricated micro-/nanostructures, such as laser-induced welding/sintering and fragmentation, would be significant if the micro-/nanostructures have strong absorption at the laser wavelength, for example, due to surface plasmon resonance. Secondary laser processing could also have a larger impact on the morphology of the products with the increasing of ablation time. The pulse duration, frequency, and fluence will determine the ablation mechanism as discussed in Section 2.4, which has the fundamental influence on the particle formation.

The products are usually solid spheres. However, other morphologies have also been observed, such as hollow particles, cubes, rods/spindles/tubes, disks/plates/sheets, and more complex structures, which will be specified in the follow sections. Among these micro-/nanostructures, some were fabricated with the assistance of external factors, such as templates and electrical field, while the others were formed directly by PLAL. In the case of non-spherical particles, the crystal structure and the surfactants in the liquid could strongly affect the morphologies. The particles may exhibit some crystal facets or facet combinations to decrease the surface free energy, and the surfactants could selectively adsorb on certain

Table 1
Pulsed laser ablation of typical materials in liquid media[a].

Target	Liquid medium	Laser type, wavelength, pulse duration, frequency, fluence (or energy per pulse), ablation time (or pulse number)	Product (size and note)
Ag	Water, acetone, or methanol	Nd:YAG, 1064 nm, N/A, 10 Hz, 55 mJ, 10 min	Ag colloid (10–50 nm; note: also prepared Au, Pt, and Cu colloids) [8]
	Water	Cu vapor, 510.6 nm, 20 ns, 15 kHz, 10–30 J/cm^2, 2 h	Ag NPs including disk-like NPs (also produced Au NPs) [97]
	Water, ethanol, or dichloroethane	Cu vapor, 510.6 nm, 20 ns, 15 kHz, 1–2 J/cm^2, N/A	Ag NPs (~60 nm; note: also produced Au, Ti, and Si NPs) [98]
	Water or acetone	N/A, 1030 nm, <10 ps, 200 kHz, 250 μJ, 30 s	Ag NPs (<10 nm; note: also produced Cu, Mg, and ZrO$_2$ NPs) [22]
	C-1 to C-5 alcohols	Nd:YAG, 1064 or 532 nm, 6 ns, 10 Hz, ~1 J/cm^2, 1–5 min	Ag NPs (observed chain-like segments; note: the starting materials were Ag flakes) [99]
	Water + SDS	Nd:YAG, 532 nm, 10 ns, 10 Hz, <90 mJ, <10^5 shots	Ag NPs [9,100]
	Water + NaCl + phtalazine or 2,2'-bipyridine	Nd:YAG, 1064 nm, 40 ps, 1 Hz, 40 mJ, 30 min	Ag colloid [101,102]
	Water + NaCl	Nd:YAG, 1064 nm, 20 ns, 10 Hz, 10–30 mJ, 15–240 min	Ag NPs (6–70 nm) [103]
	Water + NaCl	Nd:YAG, 1064 nm, 5 ns, 10 Hz, 6.4 J/cm^2, 5 min	Ag NPs (5–50 nm in 5 mM NaCl solution) [104]
	Water + NaCl	KrF, 248 nm, 30 ns, 10 Hz, 7.5–15.0 J/cm^2, 5–20 min	AgCl cubes and Ag clusters when the NaCl concentration ≤0.01 M [89]
	Water + CTAB, TTAB, or STAB	Nd:YAG, 355 nm, 7 ns, 10 Hz, 100 mJ, 30 min	Layered nanocomposites of AgBr and cationic surfactant molecules [105]
	Water + PVP	Nd:YAG, 1064 nm, 8 ns, 10 Hz, 12 mJ, 10 min	Ag NPs (<30 nm) [106]
	Water + polysorbate 80	KrF, 248 nm, 30 ns, 10 Hz, ~8.8 J/cm^2, 20–80 min	A mixture of Ag$_2$O cubes, pyramids, triangular plates, pentagonal rods, and bars, as well as Ag spheres [23]
	DMSO	Nd:YAG, 532 nm, 15 ns, 1 Hz, 10 J/cm^2, 2 h	Ag$_2$S NPs [107]
	Water + SC + PVP	Ti/sapphire, 800 nm, 80 fs, 250 kHz, N/A, 10 min	Ag thin films with ultrasmall nanopores (~2 nm) [108]
Au	Water + SDS	Nd:YAG, 1064 nm or 532 nm, 10 ns, 10 Hz, ≤90 mJ, <10^5 shots	Au NPs [36,109–112] (note: observed [110,111] and studied the mechanism [112] of laser-induced size-reduction of Au NPs, found laser-induced formation of Au nano-networks [36])
	Water, water + NaCl, KCl, NaNO$_3$, HCl or NaOH, n-propylamine	Ti/sapphire, 800 nm, 120 fs, 1 kHz, 0.2 mJ, N/A	Au NPs (note: surface chemistry was studied) [90]
	Water, water + α-CD, β-CD, or γ-CD, water + β-CD + NaCl + HCl or NaOH	Ti/sapphire, 800 nm, 110 fs, 1 kHz, ≤1 mJ, N/A	Au NPs [113–115]
	Supercritical CO$_2$	Nd:YAG, 532 nm, 9 ns, 20 Hz, 0.8 J/cm^2, 5 min	Au NPs in a liquid-like density of CO$_2$, and Au nano-networks in a gas-like density of CO$_2$ [116]
	Water, water + CTAB	Ti/sapphire, 800 nm, 100 fs, 1 kHz, 300 μJ, 20 min	Au NPs (5.3 ± 2.1 nm in CTAB solution, and 11.9 ± 7.8 nm in water) [58]
	Water + penetratin	Ti/sapphire, 800 nm, 120 fs, 5 kHz, 100 μJ, 106 s	Penetratin-conjugated Au NPs [117]
Pt	Water + SDS	Nd:YAG, 1064 or 532 nm, 10 ns, 10 Hz, 1.6–3.0 J/cm^2, ≤6000 shots	Pt NPs [118] (note: By 355 nm laser irradiation of Pt NPs coated with SDS, Pt nano-networks have been produced [37])
	Water	Nd:YAG, 1064 nm, 10 ns; 532 nm, 8 ns; or 355 nm, 7 ns, N/A, 1–110 J/cm^2, 15 min	Pt NPs [92,119,120]
	Water, water + SDS	KrF, 248 nm, 30 ns, 10 Hz, 2.3–6.8 J/cm^2, 10 min	Solid and hollow Pt micro-/nanoparticles, and hollow Pt aggregates [121]
Zn	Water + SDS	Nd:YAG, 355 nm, N/A, 10 Hz, ≤100 mJ, 1 h	Layered nanocomposite of β-Zn(OH)$_2$ and zinc dodecyl sulfate [88,122]
	Water + SDS, CTAB, LDA, or OGM	Nd:YAG, 355 nm, 5–7 ns, 10 Hz, 6.7 J/cm^2, 1 h	Layered nanocomposite of β-Zn(OH$_2$ and zinc dodecyl sulfate in SDS solutions, and ZnO NPs in all the other solutions [123]
	Water + ethanol + SDS	KrF, 248 nm, 30 ns, 10 Hz, 4.3 J/cm^2, 20 min	Self-assembled layers of β-Zn(OH)$_2$ and zinc dodecyl sulfate [124]
	Water + SDS	Nd:YAG, 532 nm, 15 ns, 10 Hz, 100 mJ, 0.5–5 h	ZnO NPs, including nanoleaf depending on the SDS concentration and ablation time [125]
	Water, water + SDS	Nd:YAG, 1064 nm, 10 ns, 10 Hz, 35–70 mJ, 30 min	Zn/ZnO core/Shell NPs (note: tree-like NSs were obtained by aging the corresponding colloids) [87,126–128]
	Water, water + LDA or CTAB at 80 °C	Nd:YAG, 355 nm, 7 ns, 10 Hz, 3.2 J/cm^2, 40 min	ZnO nanorods [129]
	Water + CTAB	Nd:YAG, 355 nm, 7 ns, 10 Hz, 100 mJ, 20 min	ZnO NPs (note: spindle-like aggregates were obtained by aging the corresponding colloids) [130]
	THF	Trumpf TruMicro 5250, 515 nm, 7 ps, 125 μJ, N/A	Zn/ZnO NPs (<15 nm) [131]
	H$_2$O$_2$, H$_2$O$_2$ + SDS, CTAB or OGM	Nd:YAG, 355 nm, 8 ns, 10 Hz, 130 mJ, 60 min	ZnO$_2$ NPs (4–40 nm) [132]
	Water + ethanol	KrF, 248 nm, 30 ns, 10 Hz, 8.4 J/cm^2, 10 min	Zn/ZnO NPs and hollow aggregates [133]
	ME, DM, water + ethanol, water + ethanol + ferrocene	Nd:YAG, 1064 nm, 0.6–1 ms, 1 Hz or 20 Hz, 10^6 W/cm^2, 5 min	Zn/ZnO core/shell NPs, hollow ZnS or ZnO NPs, or solid ZnS NPs depending on the liquid media and laser frequency [57,134]
Ti	Water, water + SDS	Nd:YAG, 355 nm, N/A, 10 Hz, 150 mJ, 60 min	TiO$_2$ NPs [135,136]

Table 1 (*Continued*)

Target	Liquid medium	Laser type, wavelength, pulse duration, frequency, fluence (or energy per pulse), ablation time (or pulse number)	Product (size and note)
	Water	Nd:YAG, 532 nm, 15 ns, 2 Hz, 4.1–12.4 J/cm^2, 30 min	TiO$_x$ NPs [137]
	Water + PVP	Nd:YAG, 1064 nm, 10 ns, 10 Hz, 80 mJ, 60 min	Rutile TiO$_2$ NPs [138]
	Water	Nitrogen, 337 nm, 10 ns, 10 Hz, 50 J/cm^2.	TiO$_2$ NPs (~10 to 100 nm) [139]
	Water, water + SDS	Nd:YAG, 355 nm, N/A, 10 Hz, 150 mJ, 60 min	TiO$_2$ NPs [135,136]
Al	Ethanol, EG, or acetone	Nd:YAG, 1064 nm, 6 ns, 10 Hz, 280–400 mJ, 5–15 min	Al NPs [140]
	Ethanol	Ti/sapphire, 800 nm, 200 fs, 1 kHz, 0.2–0.5 J/cm^2, 10 min; and Nd:YAG, 1.06 μm, 30 ps or 150 ps, 10 Hz, 8 J/cm^2 or 1.5 J/cm^2, 1 h	Al NPs (10–60 nm), some of them contain irregular cavities [141]
	Water, water + ethanol	KrF, 248 nm, 30 ns, 10 or 20 Hz, 2.3 J/cm^2 or 4.6 J/cm^2, 5 min	Solid and hollow Al$_2$O$_3$ micro-/nanoparticles [66]
	Water	Nd:YAG, 1064 nm, 8 ns, 10 Hz, 10–55 J/cm^2, 60 min	Al/Al$_2$O$_3$ NPs [142]
	Water	Nd:YAG, 1064 nm, 16 ns, 10 Hz, 850 mJ, 5 min	(H$^+$, Al^{2+})-doped Al$_2$O$_3$ NPs [143]
	THF + oleic acid	Nd:YAG, 1064 nm, 6 ns, 20 Hz, 0.88 J, 5 min	Al NPs [144]
Mg	Water, water + SDS	Nd:YAG, 355 nm, 7–8 ns, 10 Hz, 100 J/cm^2, 60 min	wormhole-like Mg(OH)$_2$ NSs in water, tube-, rod- or platelet-like Mg(OH)$_2$ NSs in SDS solutions [145]
	Acetone, 2-propanol, water, water + SDS	Nd:YAG, 1064 nm, 5.5 ns, 10 Hz, 0.265 J/cm^2, 60 min	MgO and Mg NPs in acetone and 2-propanol, fiber-like Mg(OH)$_2$ NSs in water, rod-like, triangular, and plate-like Mg(OH)$_2$ NSs in SDS solutions [146]
	Ethanol, ethanol + n-hexane	Nd:YAG, 1064 nm, 0.6–1 ms, 1 Hz, 10^6 W/cm^2, 5 min	Mg NPs, MgO nanocubes or hollow NPs [57,134]
	Water, water + SDS or SC	KrF, 248 nm, 30 ns, 10 Hz, 3.2–15 J/cm^2, 0.5–20 min	Mg(OH)$_2$ layers and hollow MgO particles in water, hollow MgO particles in water with SDS or SC [147]
Pb	DM, DM + n-hexane, MA, ME	Nd:YAG, 1064 nm, 0.6–1 ms, 1 or 20 Hz, 10^6 W/cm^2, 5 min	Pb/PbS core/shell NPs and heterostructures, PbS nanocubes or hollow NPs depending on the liquid media and laser frequency [57,134]
Cu	Water	Nd:YAG, 532 nm, 10 ns, 5 Hz, 100 mJ, 60 min	CuO nanospindles (*note*: applied electrical field to the liquid) [148]
	1-Dodecanethiol	Nd:YAG, 1064 nm, 1 ms, 20 Hz, 10^6 W/cm^2, 5 min	CuS nanowires [57,134]
	Water + ethanol	Nd:YAG, 1064 nm, 0.6 ms, 1 Hz, 10^6 W/cm^2, 5 min	Hollow CuO NPs [134]
	Water	Nd:YAG, 532 nm, 10 ns, N/A, 9–500 J/cm^2, N/A	CuO NPs (≤200 nm) at 500 J/cm^2, CuO/Cu$_2$O composites at 80 J/cm^2, Cu/Cu$_2$O composites at 9 J/cm^2 (*note*: fluence was adjusted by changing the focusing condition) [149]
	Water, acetone, water + 1,10-phenanthroline or 4,40-bipyridine	Nd:YAG, 532 or 1064 nm, ~10 ns, 10 Hz, 2.5 J/cm^2, 10–30 min	Cu colloidal suspensions with surface complexes in aqueous solution of ligands [150]
Fe	Water + PVP	Nd:YAG, 1064 nm, 10 ns, 10 Hz, 80 mJ, 60 min	FeO NPs [151]
	Water + ethanol	Nd:YAG, 1064 nm, 1 ms, 1 Hz, 1000 J/cm^2, 5 min	Fe/Fe$_x$O$_y$ core/shell NPs [57]
	THF, AN, DMF, DMSO, toluene, ethanol	Nd:YAG, 1064 nm, 9 ns, 10 Hz, 5 J/cm^2, N/A	α-Fe, iron oxide (magnetite/maghemite), iron@iron oxide, and Fe$_3$C depending on the solvent [152]
Ni	EG + PVP	Nd:YAG, 532 nm, 3 ns, 20 Hz, 6.37 J/cm^2, 60 min	Ni NPs (<11 nm; *note*: also produced Co and Ni-Co NPs) [153]
	Water	Nd:YAG, 1064 nm, 1 ms, 20 Hz, 1000 J/cm^2, 5 min	NiO nanocubes [57]
Mn	Water	Nd:YAG, 1064 nm, 10 ns, N/A, 80 mJ, 30 min	Mn$_3$O$_4$ NPs (7.1–9.2 nm) [154]
W	Ethanol	CuHBr vapor, 510 and 578 nm, 30 ns, 13 kHz, 90 J/cm^2, 30 min	W particles (0.05–0.5 μm) [155]
	Water	Nd:YAG, 532 nm, 5 ns, 10 Hz, 1–7 J/cm^2, 1–2 h	WO$_{3-x}$ NPs (<20 nm with the presence of spherical aggregates about 80–100 nm in size) [156]
Sn	Water, water + SDS	Nd:YAG, 355 nm, N/A, 10 Hz, 100 mJ, 60 min	SnO$_{2-x}$ NPs (2–3 nm) in the 0.01 M SDS solution [157]
C (graphite)	Water, acetone	Nd:YAG, 532 nm, 10 ns, 5 Hz, 100 J/cm^2, 30–45 min	Diamond NPs [158,159]
	Ammonia	Nd:YAG, 532 nm, 15 ns, 10 Hz, 15 J/cm^2, 2–5 h	α-C$_3$N$_4$ NPs and nanorods [160]
	Water	Ti:Sapphire, 800 nm, 100 fs, 1–1000 Hz, 2.7 mJ, 2000 pulses	diamond-like carbon (DLC) when the frequency of 10 or 100 Hz, nano-diamonds and DLC when frequency of 1000 Hz [161]
C (amorphous)	Water + ethanol + acetone + KCl or NaCl	Nd:YAG, 532 nm, 10 ns, 10 Hz, 100 J/cm^2, 15 min	C micro-/nanocubes with C$_8$-like structure [162]
C$_{60}$	Water	Nd:YAG, 532 nm, 14 ns or 355 nm, 8 ns, 10 Hz, 20–200 mJ/cm^2, 10 min	C$_{60}$ aqueous nanocolloids (~20 to 60 nm) [163]

Table 1 (*Continued*)

Target	Liquid medium	Laser type, wavelength, pulse duration, frequency, fluence (or energy per pulse), ablation time (or pulse number)	Product (size and note)
Si	Water	Nd:YAG, 355 nm, 8 ns, 30 Hz, 0.07–6 mJ, 30 min	Si NPs (2–50 nm prepared at 6 mJ) [164]
	Ethanol	Ti/sapphire, 800 nm, >35 fs, 1 kHz, 4 J/cm^2, 10 min	Si NPs (~30 to 100 nm) [165]
	Water, water + SDS, ethanol, water + ethanol	Nd:YAG, 1064 nm, 10 ns, 10 Hz, 50–200 mJ, 30–60 min	Si NPs (<40 m) [166,167]
	Water + AgNO$_3$	Nd:YAG, 355 nm, <40 ns, 30 Hz, <40 J/cm^2, 2 min	Ag-SiO$_2$ core–shell NPs; *note*: also studied targets of Ge and W, and aqueous solutions of HAuCl$_4$ or a mixture of HAuCl$_4$ and AgNO$_3$ [168]
	Chloroform	Nd:YAG, 355 nm, 40 ns, 5 kHz, ~40 J/cm^2, N/A	Polycrystalline Si particles (~20 to 100 nm); ultrasonic post-treatment of these particles in the presence of HF produced Si NPs (3–5 nm) [169]
Ge	Water	Nd:YAG, 532 nm, 10 ns, 5 Hz, 150 mJ, 180 min	GeO$_2$ micro-/nanocubes and spindles (cubes 200–500 nm, spindles 200–400 nm, note: applied electrical field and ultrasonic oscillation) [170]
	Toluene	Nd:YAG, 532 nm, 10 ns, 1 Hz, 100 J/cm^2, 60 h	Ge NPs of tetragonal phase (<30 nm) and cubic phase (>200 nm) (*note*: applied electrical field) [171]
Ni–Fe alloy	Water + SDS	KrF, 248 nm, 30 ns, 20 Hz, 7 J/cm^2, 20 min–9 h	Ni–Fe particles (partially oxidized) and hollow aggregates depending on ablation time [25]
	Cyclopentanone	Ti/sapphire, 800 nm, 120 fs, 5 kHz, 300 μJ, 10–80 min	Ni–Fe NPs (<100 nm; note: also produced Sm–Co NPs) [172]
Ag–Au alloy	Water	Nd:YAG, 1064 nm, 6 ns, 10 Hz, 50 mJ, 30 min	Au–Ag alloy NPs (~10 nm) [173]
Ag and Au	Water	Nd:YAG, 1064 nm, 6–9 ns,5 Hz, 300 mJ, 30 min of Ag and 30–150 min of Au	Ag core/Au shell NPs (*note*: Ag target was first ablated, and then replaced by Au target) [174]
TiO$_2$	Water, ethanol, cyclohexane	Nd:YAG, 532 nm, 8 ns, 10 Hz, 100–250 mJ, 5 min	TiO$_2$ NPs [175]
α-Al$_2$O$_3$	Water	Nd:YLF, 1047 nm, 20–60 ns, 4–15 kHz, ≤4.6 mJ, 5–30 min	α-Al$_2$O$_3$ NPs (~30 ± 29 nm) [17]
CdS	Water	Ti/sapphire, 800 nm, 100 fs, 1 kHz, 800 J/cm^2, 5 min	CdS NPs (<10 nm) [176]
Ca$_{10}$(PO$_{4\ 6}$(OH)$_2$	Water	Nd:YAG, 355 nm, 5–7 ns, 30 Hz, 10 J/cm^2, N/A	Ca$_{10}$(PO$_4$)$_6$(OH)$_2$ NPs (5–20 nm) [177]
Y$_2$O$_3$:Eu^{3+}	Water	Nd:YAG, 355 nm, 5 ns, 10 Hz, N/A, 2–3 h	Y$_2$O$_3$:Eu^{3+} NPs (5–10 nm; *note*: also produced Lu$_2$O$_2$S: Eu^{3+}, Gd$_2$SiO$_5$:Ce^{3+}, Lu$_3$TaO$_7$: Gd^{3+}/Tb^{3+} NPs) [178]
	Water + MEEAA	Nd:YAG, 355 nm, 5 ns, 10 Hz, 7 mJ, 20–120 min	Y$_2$O$_3$ NPs with bridging bidentate (<3 nm; note: also ablated Gd$_2$O$_3$: Eu^{3+} and Y$_3$Al$_5$O$_{12}$: Ce^{3+} targets) [179]
Tb$_3$Al$_5$O$_{12}$:Ce^{3+}	Water, water + LDA	Nd:YAG, 355 nm, 5–7 ns, 10 Hz, N/A, N/A	Tb$_3$Al$_5$O$_{12}$:Ce^{3+} NPs (<25 nm in water, <15 nm in LDA solution) [180]

[a] *Abbreviations in the table*: sodium citrate (SC), cetyltrimethylammonium bromide (CTAB), tetradecyltrimethylammonium bromide (TTAB), stearyltrimethylammonium bromide (STAB), cyclodextrin (CD), lauryl dimethylaminoacetic acid betaine (LDA), octaethylene glycol monododecyl ether (OGM), ethylene glycol (EG), dodecyl mercaptan (DM), mercaptoacetic acid (MA), mercaptoethanol (ME), tetrahydrofuran (THF), acetonitrile (AN), dimethylformamide (DMF), dimethylsulfoxide (DMSO), 2-[2-(2-methoxyethoxy) ethoxy]acetic acid (MEEAA).

facets, which restrains crystal growth in the related directions, resulting in complex structures.

3.2. Hollow particles

Hollow micro-/nanostructures have attracted enormous interest due to their unique properties such as the high surface-to-volume ratio, low density and coefficients of thermal expansion, which have found applications in catalyst support, rechargeable batteries, sensing, drug delivery, and biomedical imaging [183]. We found that by 248 nm excimer laser ablation of bulk Pt [121], Al [66,184], Mg [147], Ag [23,133,185], Cu [186], Zn [133], Si [133], Fe–Ni alloy [25,133], TiO$_2$ [121], and Nb$_2$O$_5$ [121], in water, water/ethanol mixtures or aqueous solutions of surfactants, hollow micro-/nanoparticles or aggregates with sizes up to micrometers could be generated. Fig. 7(A and B) and (C and D) shows the hollow Al$_2$O$_3$ particles and hollow Pt aggregates, respectively. These hollow particles and aggregates are considered to form

on laser-induced bubbles via bubble surface pinning by laser-produced clusters or particles [66,133,147,184], and a detailed mechanism can be found in [147]. In this hollow particle formation scenario, thermodynamic and kinetic requirements must be satisfied. Kinetically, the bubble surface needs to trap enough clusters to form a shell, and the clusters mainly come from the liquid. And thus the clusters, undergoing Brownian motion, should have enough time to diffuse to the bubble interface, which in turn, require a long lifetime of the bubble. Compared with the other materials we have studied, Al and Mg targets are more likely to generate hollow particles in water [66,147]. The reason is both of them are highly reactive, and generate atomic and/or molecular hydrogen gas by the oxidation in water. The gas may not only provide cavitation nuclei for the laser-produced bubbles, but also increase the stability of the bubbles as shown in Section 2.5. Another observation is adding ethanol to water could promote the formation of hollow particles, and it is shown that bubbles in the water–ethanol have longer lifetimes [133,184]. This phenomenon may be related to the lower
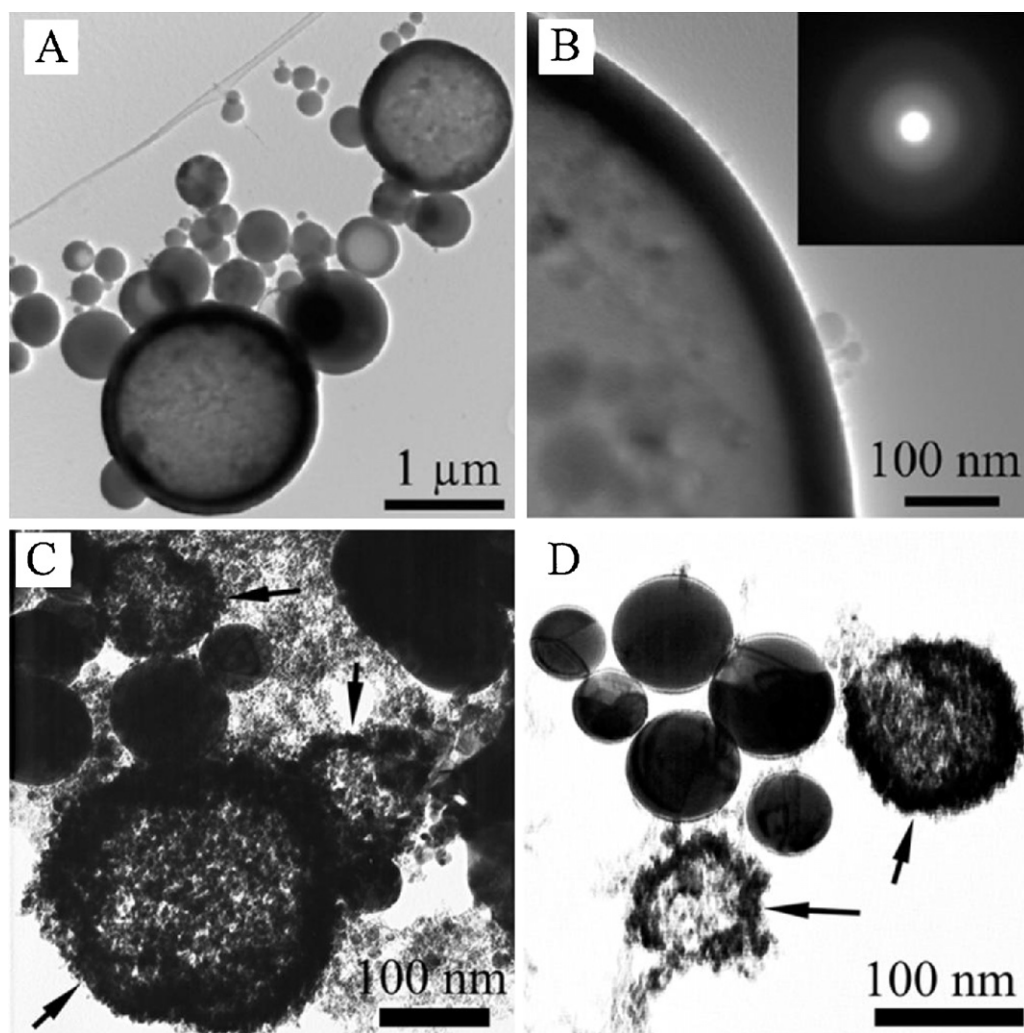
Fig. 7. TEM images of (A) solid and hollow Al_2O_3 particles fabricated by excimer laser ablation of Al in water, and (B) the shell of a hollow sphere with the corresponding selected area electron diffraction (SAED) pattern shown in the inset. Adapted with permission from [66]. Copyright 2010 American Chemical Society. (C) and (D) Pt particles fabricated by excimer laser ablation of Pt in water. The arrows indicate typical hollow Pt sphere assembled from smaller nanoparticles.
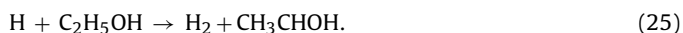
Source: Adapted with permission from [121].

© 2010 Institute of Physics.

boiling point of ethanol and the microscopic phase separation of water–ethanol clusters. Another reason is the photodissociation of water molecules by the 248 nm excimer laser:

$$H_2O \xrightarrow{2h\nu} OH + H, \tag{24}$$

and the reaction of hydrogen radicals with ethanol to form hydrogen gas [187]:

$$H + C_2H_5OH \rightarrow H_2 + CH_3CHOH. \tag{25}$$

Specifically, the observation of hollow Pt particles may be partly due to the catalytic effect of Pt to the photodissociation of water [188].

Thermodynamically, an energy barrier to hinder a trapped cluster from escaping into the liquid must exist,

$$E_b = \pi r^2 (1 - \cos \theta)^2 \gamma_{LB}, \tag{26}$$

where r is the radius of the cluster, γ_{LB} is the surface tension of the bubble interface, and θ is the contact angle of the nanoparticle with the liquid, and E_b should be larger than the thermal energy of the cluster [133,147]. Since the typical contact angle of water on a metal surface is 20° and 30–40° on an oxide surface as mentioned

in Section 2.5, the energy barrier may keep metal and oxide clusters on the bubble interface. In the case of very hydrophilic clusters, such as hydroxides which give $E_b \approx 0$, hollow particles will not form via bubble surface pinning. This is in agreement with our observation that MgO could form hollow particles by pulsed laser ablation of Mg in water but Mg(OH)$_2$ did not [147].

Similar hollow particles have been observed in the products of pulsed laser ($\lambda = 800$ nm) ablation of Ti target in water [189], and in the products of pulsed laser ($\lambda = 1047$ nm) ablation of α-Al_2O_3 in water [17]. And very recently, Yang et al. reported the fabrication of hollow carbon and carbide particles by pulsed laser ($\lambda = 1064$ nm) ablation of tungsten or silicon targets in ethanol or toluene [190,191], which were also considered to form on bubbles. Laser-induced bubbles are similar to acoustic cavitation bubbles, and the latter have been applied to fabricate hollow particles in a synthetic environment [192] or in a colloidal solution [193]. The merit of fabricating hollow particles by PLAL is that it can simultaneously produce the templates (bubbles) and the coating materials (clusters or particles), thus directly fabricate hollow structures from bulk materials. However, the hollow particles are usually mixed with solid particles, and it remains a challenge to control the size distribution. One possible route to improve the generation
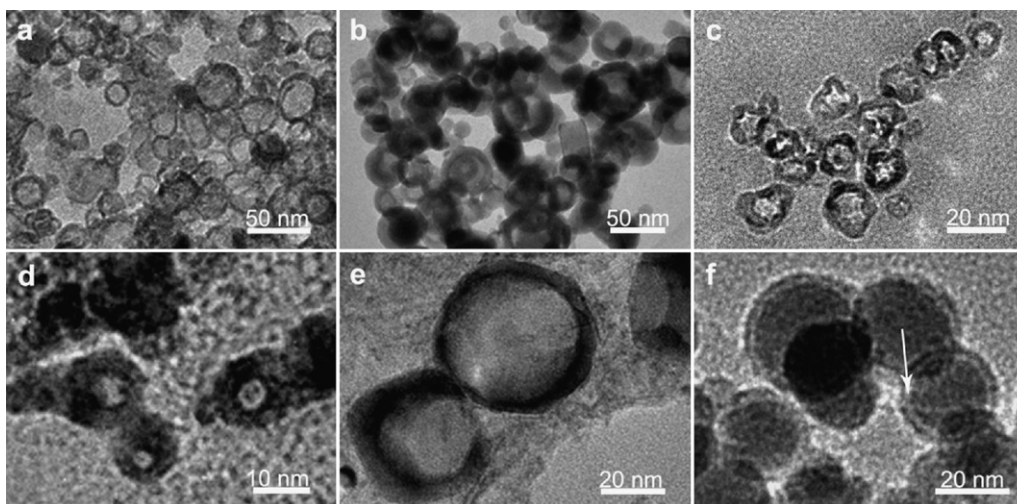
Fig. 8. TEM images of hollow nanoparticles prepared by PLAL via surface reaction of metal nanodroplets: (a) ZnS, (b) PbS, (c) MgO, (d) CuO, and (e) CoO. (f) Fe/Fe$_x$O$_y$ core/hollow shell nanospheres. The arrow indicates a gap between a metal core and an oxide shell.

Source: Adapted with permission from [134].

© 2010 American Chemical Society.

of hollow particles is to incorporate the acoustic cavitation into the laser ablation experiments by holding the target and liquid in a high-intensity ultrasonic rig. In this way, the laser-induced cavitation and acoustic cavitation can be coupled, and thus may largely promote the formation of bubbles and increase their lifetimes.

Recently, Niu et al. also obtained hollow nanoparticles with sizes smaller than 50 nm, including hollow PbS, MgO, ZnS, ZnO, CuO, CoO nanoparticles, and Fe/Fe$_x$O$_y$ core/hollow shell nanospheres (see Fig. 8) by pulsed laser (λ = 1064 nm) ablation of metallic targets in ethanol/water mixtures or organic solvents, and attributed the formation of these hollow nanoparticles to Kirkendall Effect [57,134]. It is worth noting that their experiments used a low laser power density (10^6 W/cm^2) with a long pulse width (0.6–1 ms) to generate metal nanodroplets instead of vapor or plasma, which was considered by the authors as a decisive point to make the nanoscale Kirkendall Effect possible [57]. The Kirkendall effect, first discovered by Ernest Kirkendall in 1947 [194], explained the void formation at the interface of a diffusion

couple considering the different interdiffusion rates between two components. The net flow of mass was balanced by an opposite flux of vacancies, which finally condensed into voids. Similar effect in the nanoscale was employed by Yin et al. to explain the formation of hollow compound nanoparticles, such as cobalt sulfate nanoshells by reaction of cobalt nanocrystals with sulfur [195]. In this mechanism, the diffusion of the metal core must be faster than the shell component; otherwise cracked shell will form instead of hollow interior [195]. Also because some voids exist between the metal core and the shell during the process, the mass transport needs the formation of core–shell bridges and considerable surface diffusion [195,196], both of which more likely occur in the nanoscale and thus the hollow nanoparticles generated by this methods are generally very small [183], e.g., <20 nm in Yin et al.'s research [195]. The nanoscale Kirkendall Effect could not explain the formation of hollow metallic particles, such as hollow Pt particles [121], nor hollow particles from oxide targets, such as Al$_2$O$_3$ [17], TiO$_2$ [121], and Nb$_2$O$_5$ [121], and even some reactive targets, such as Al. Nakamura et al. have found some
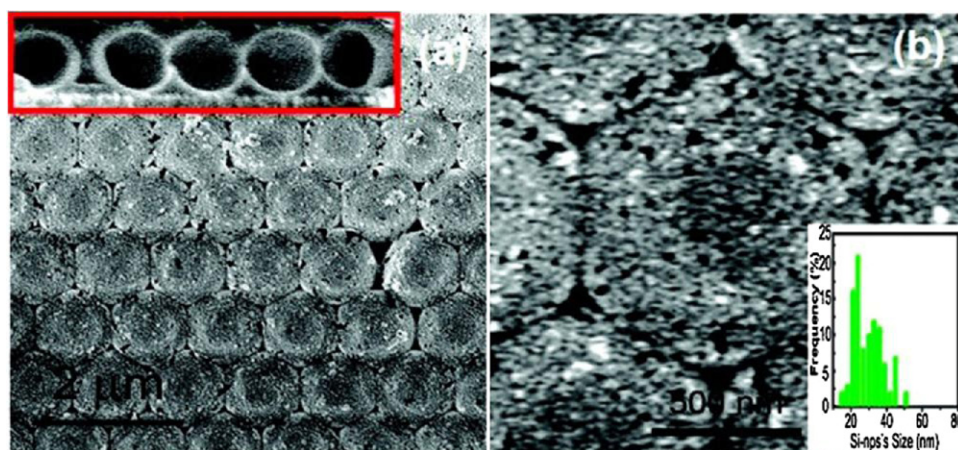

Fig. 9. Si hollow spheres array fabricated by electrophoresis of laser-produced colloids onto polystyrene spheres: (a) SEM image of the Si hollow spheres after removal of polystyrene spheres. Inset: Corresponding local cross section. (b) Local magnified image of (a). Inset: Size distribution of Si nanoparticles in the shell layer.

Source: Adapted with permission from [198].

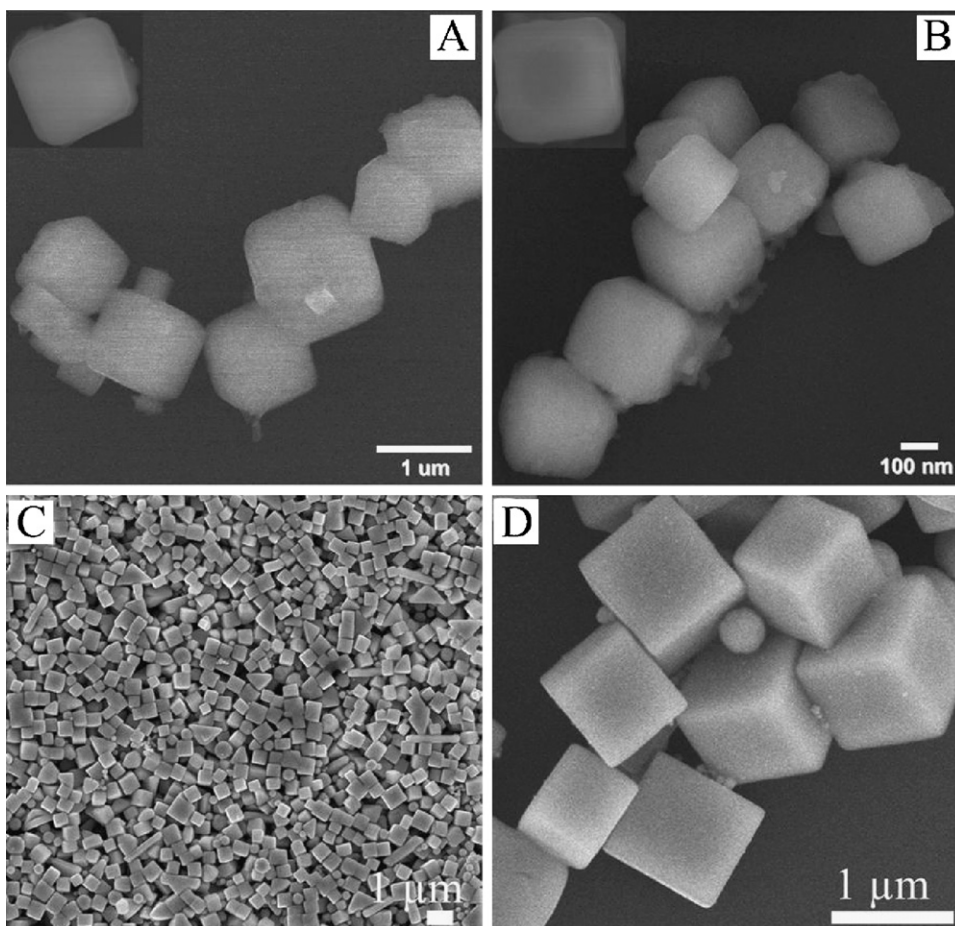© 2009 American Chemical Society.

Fig. 10. (A) and (B) SEM images of carbon micro- and nanocubes fabricated by PLA of amorphous carbon in liquid. Adapted with permission from [162]. Copyright 2008 American Chemical Society. (C) and (D) SEM images of Ag$_2$O cubes fabricated by PLA of Ag in aqueous solution of polysorbate 80.
Source: Adapted with permission from [23].
© 2011 American Chemical Society.

critical sizes of metal nanocrystals in order to form hollow metal oxide nanoparticles through the oxidation process [197]. For Al, the sizes must be smaller than 8 nm and the formation of oxide layer on Al surface stops once it reaches a critical thickness of ~1.5 nm [197]. Nevertheless, the combination of nanoscale Kirkendall

Effect and PLAL is a good route to fabricate certain types of hollow nanoparticles.

Stratakis et al. have used pulsed lasers (wavelengths from fs to ns) to ablation Al in ethanol, and observed that some particles in the products contained irregular cavities, which were considered
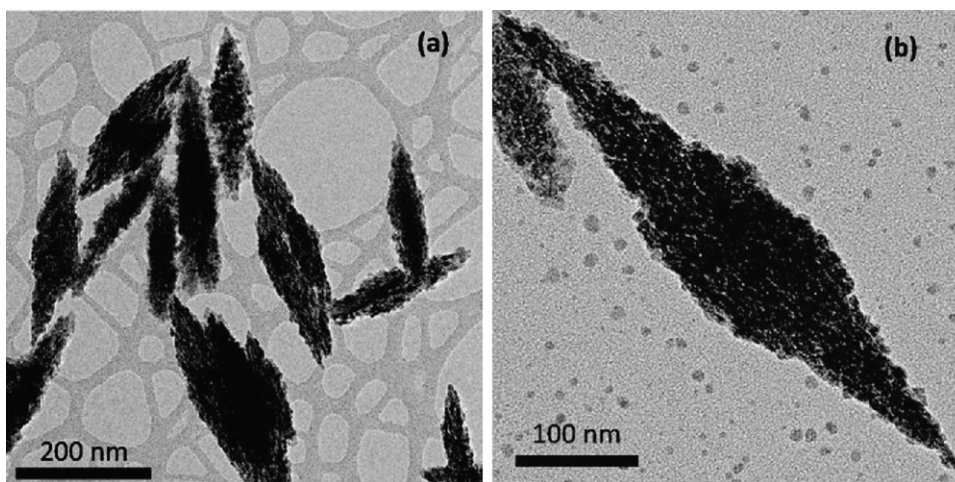

Fig. 11. TEM image of (A) CuO nanospindles synthesized by electrical-field-assisted PLA of Cu in water, (B) an individual CuO nanospindle.
Source: Adapted with permission from [148].
© 2009 American Chemical Society.

to form by the releasing of dissolved gas in molten Al during the cooling [141]. Further experiments were conducted by PLA of Al in liquid ethanol saturated with H_2, and similar cavities were observed in some particles [199]. Yang et al. also reported a route to fabricate hollow spheres by electrophoresis of Si colloids produced by PLAL [198]. The charged colloids could be coated on a polystyrene colloidal monolayer at the cathode, forming hollow shell arrays (Fig. 9). Polystyrene particles are conventional hard templates for the preparation of hollow structures [183] and the method itself does not reflect the underlying interactions of PLAL, but the post-processing of the laser-produced colloids by electrophoresis has provide a new route to fabricate complex nanostructures since the laser generated metal and semiconductor nanoparticles are usually charged [94]. Later, this method has been used by He et al. to fabricate three-dimensional (3D) netlike porous Au films on ITO glass, as well as 3D porous films from other materials, such as C, Ag, Au_xAg_{1-x}, and mixtures of Au and Ag [200].

3.3. Cubic particles

Cubes are good building blocks of self-assembly for superstructures and mesocrystals, and due to the exposure of certain facets, they are also good candidates to study the surface-related properties [201,202]. PLAL has shown the ability to produce cubic particles under some experimental conditions. Liu et al. have used electrical-field-assisted PLA of Ge in water to fabricate GeO_2 micro-/nanocubes [170]. They also synthesized carbon micro- and nanocubes (Fig. 10A and B) with C_8-like structure by PLA of amorphous carbon in a mixed solution of water, ethanol and acetone with the addition of inorganic salts such as KCl or NaCl, and considered the cubic morphology was caused by the salt ions [162]. Similar effect was observed by excimer laser ablation of Ag in aqueous solutions of NaCl, where micro- and nanocubes of AgCl were produced [89]. However, we further found that Ag_2O cubes (Fig. 10C and D) as well as other morphologies could be generated by excimer laser ablation of Ag in aqueous solution of nonionic surfactants, such as polysorbate 80, indicating that the formation of
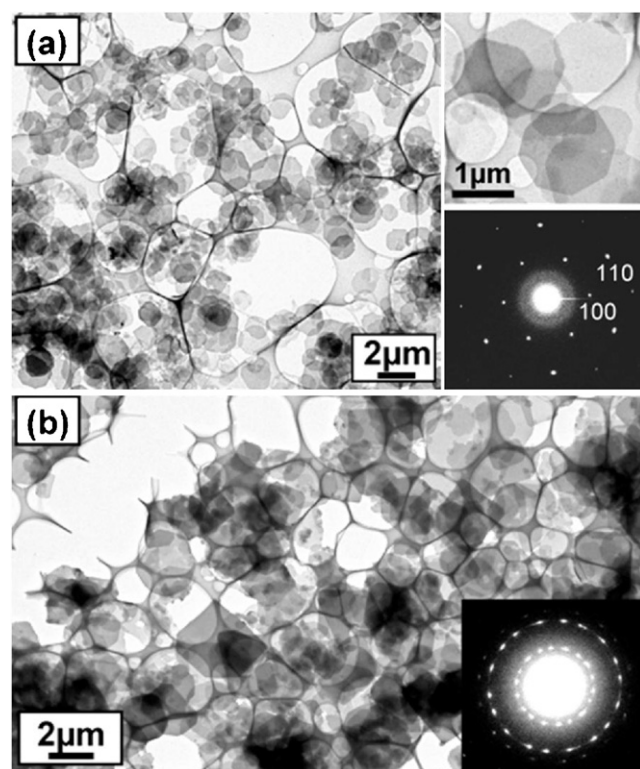

Fig. 12. TEM images of lamellar zinc hydroxide/dodecyl sulfate platelets (A) from 0.001 M or 0.01 M SDS solutions and (B) from 0.1 M SDS solution. Attached images in (A) are an enlarged morphology of a single platelet with an octagonal shape and the electron diffraction pattern from a single platelet. Inset in (B) presents the ED pattern from a gradually crumpled platelet during recording.

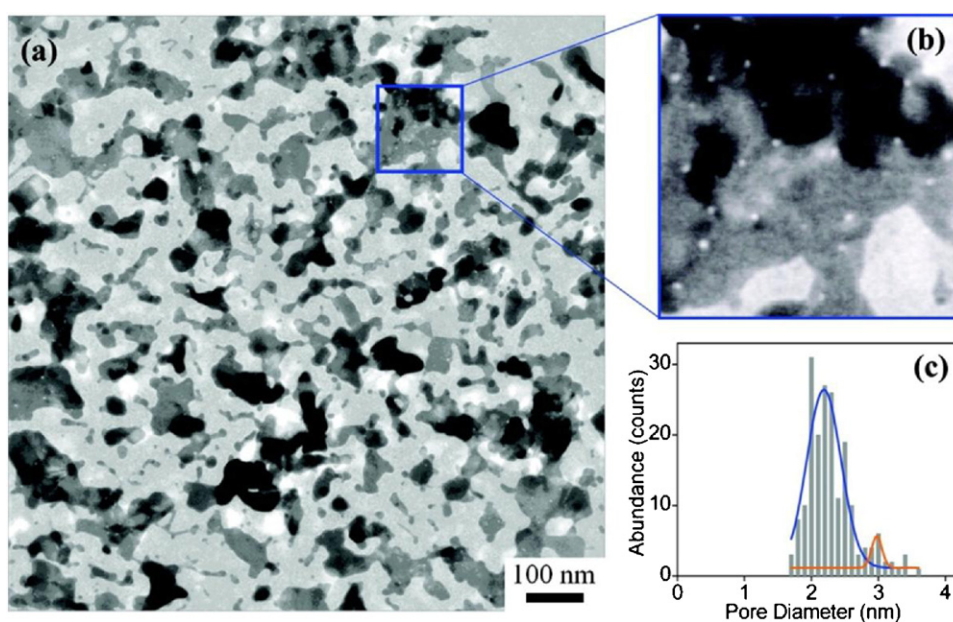*Source*: Adapted with permission from [88].

© 2004 American Chemical Society.

Fig. 13. Morphology and size distribution of the ultrasmall silver nanopores produced by femtosecond laser ablation in a capping agent solution. (a) Large area TEM image of the silver thin films. (b) Zoom-in view of the silver film with dense ultrasmall nanopores clearly visible. (c) Histogram of the diameter distribution of the nanopores in (a). The blue and yellow curves are Gaussian fits of the diameter distribution as a guide to the eye.

Source: Adapted with permission from [108].
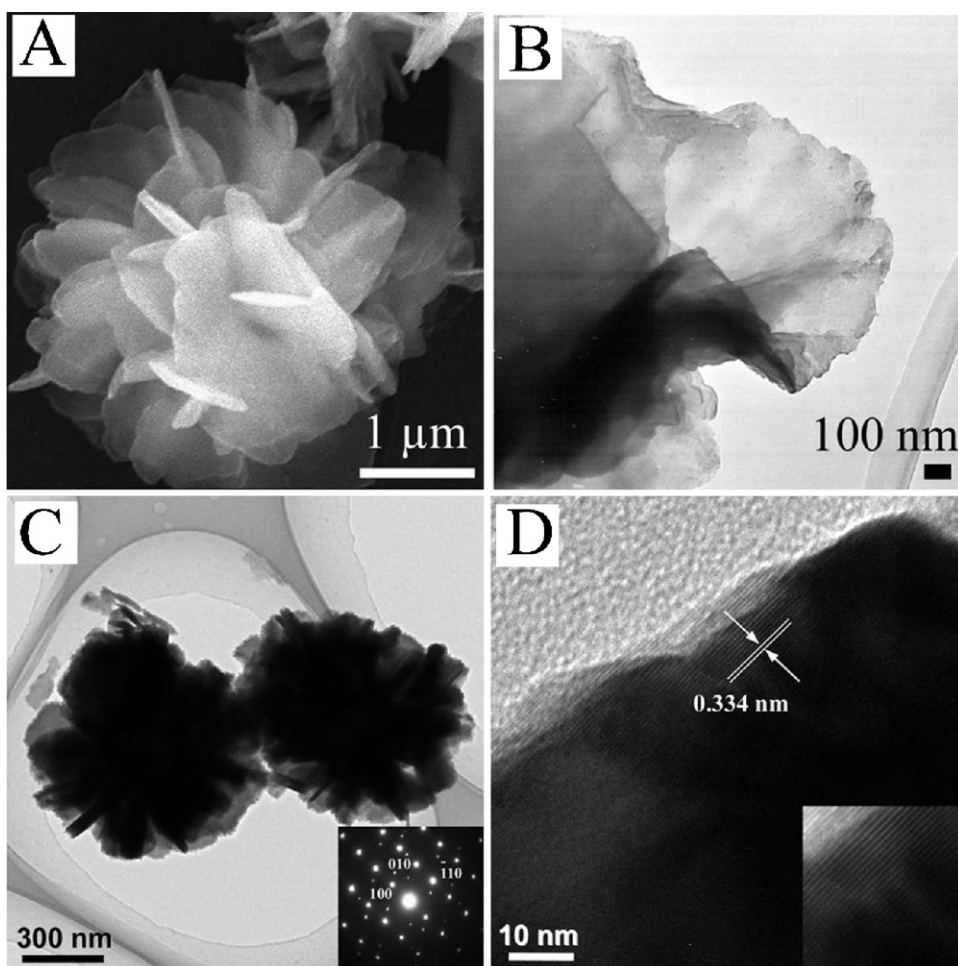
© 2011 American Chemical Society.

Fig. 14. (A) SEM and (B) TEM images of zinc hydroxide/dodecyl sulfate flower-like structures fabricated by excimer laser ablation of Zn in ethanol–water mixed solution of SDS. Adapted with permission from [124]. Copyright 2010 Elsevier. (C) TEM and (D) HRTEM images of CuVO$_7$ flower-like structures fabricated by electrochemistry-assisted laser ablation of vanadium in water using copper as electrodes. A corresponding SAED analysis is shown in the inset of (C).

Source: Adapted with permission from [96].

© 2011 American Chemical Society.

cubic morphologies may be intrinsic for some materials with cubic structures. For example, Liu and co-workers have synthesized NiO nanocubes by PLA of Ni in water, and also produced PbS nanocubes by PLA of Pb in mercaptoacetic acid and MgO nanocubes by PLA of Mg in ethanol [57]. All of the AgCl, Ag$_2$O, NiO, PbS and MgO have cubic phases, and thus it is inferred that materials with structures in the cubic crystal system may favor the formation of cubic morphology. Generally a nanocube is bounded by six {1 0 0} facets with a lower surface free energy compared to that of a nanosphere.

3.4. Nanorods, spindles and tubes

PLA also shows the ability to fabricate one-dimensional nanostructures. Typical examples are ZnO nanorods or spindles produced by PLA of Zn in water at elevated temperature or with the addition of LDA or CTAB [129,130], and the ZnO nanorods could assemble into three-dimensional clusters [129], Other examples include Mg(OH)$_2$ nanorods produced by PLA of Mg in aqueous solutions of SDS [145], and Ag$_2$O pentagonal rods and bars produced by excimer laser ablation of Ag in aqueous solution of polysorbate 80 [23]. Yang et al. have synthesized carbon nitride nanorods by PLA of graphite in ammonia solution, which could further aggregate into leaf-like and flower-like structures [160,203,204]. Recently, an electrical-field-assisted PLAL method was developed to synthesize GeO$_2$ and

CuO nanospindles (Fig. 11) from Ge or Cu in water, and the one-dimensional morphologies were considered to originate from the applied electrical field [148,170]. Formation of nanotubes by PLAL was first reported by Nistor et al., they produced boron nitride (BN) nanotubes by PLA of BN in acetone [205]. Very recently, PbS nanotubes have been fabricated by PLA of Pb in DM/n-hexane mixture [57].

3.5. Nanodisks, plates, and layers

Simakin et al. reported the fabrication of disk-like Au and Ag nanoparticles by a Cu vapor laser ablation of the respective target in water a decade ago [97]. Recently, Ag$_2$O triangular plates were produced by excimer laser ablation of Ag in aqueous solution of polysorbate 80 [23]. It is shown that PLA of Zn in aqueous solution of SDS could produce zinc hydroxide/dodecyl sulfate composite nanolayers (Fig. 12), but the formation depends on the concentration of SDS [88,122]. Similar AgBr/CTAB composite nanolayers has also been produced by PLA of Ag in aqueous solution of CTAB [105]. Mg(OH)$_2$ nanolayers have been produced by PAL of Mg in aqueous solution of SDS [145], while in this case, no evidence was shown that the surfactant was involved in the products. The ablation time is also important, as Yang et al. found PLA of Zn in aqueous solution of SDS could generate ZnO leaf-like structures only after a long ablation time [125].

Very recently, Bian et al. fabricated Ag thin films, or nanolayers, with ultrasmall nanopores by using femtosecond laser ablation of Ag target in aqueous solution of sodium citrate and poly(vinylpyrrolidone) (Fig. 13) [108]. The citrate anions selectively attached to the {1 1 1} facets of Ag particles and promoted the growth of Ag nanolayers within the (1 1 1) plane. And during the growth, the confinement of the citrate molecules by Ag nanolayers resulted in the formation of nanopores. The size of the nanopores can be adjusted by using capping agent molecules with different sizes, and this method advances the capability of PLAL in making nanostructures [108].

3.6. Complex nanostructures

There are only a few reports on three-dimensional complex nanostructures formed directly by PLAL, including the ZnO nanorod clusters and carbon nitride flower-like structures mentioned previously [129,204], which were formed by self-assembly of laser-produced nanorods. Similar self-assembly behavior has led to the formation of tree-like Zn/ZnO nanostructures by aging the laser-produced Zn/ZnO colloids [204], γ-Cd(OH)$_2$ nanotetrapods and nanoflower-like structures by PLA of Cd in aqueous solution of SDS [206], and the formation of zinc hydroxide/dodecyl sulfate flower-like structures by PLA of in ethanol-water mixed solution of SDS (Fig. 14A and B) [124]. The laser-produced colloids have been also used in electrophoresis to fabricate complex nanostructures [94,200], indicating that incorporating the laser-produced colloids with other nano-fabricating methods, such as the dip-pen nano-lithography, is a possible route to produce complex nanostructures. Using the aforementioned method of electrochemistry-assisted laser ablation in liquid, Liu et al. have also obtained CuVO$_7$ flower-like structures (Fig. 14C and D) by using vanadium as the ablation target and copper as the electrodes [96].

It is worthy noting that the chemical reactions in PLAL, which are usually intrinsic as discussed in Section 2.7, will provide a large room for investigation. One may survey the traditional chemical deposition reactions of metal ions with other anions, and ablate the metal in a solution containing the anions, novel nanostructures may be obtained.

4. Conclusions

This review has described a comprehensive mechanistic scenario of PLAL and illustrated the combinatorial library of constituents and interactions between them, including the photons, the liquid molecules, the solid target, and the laser-produced particles. Two unique phenomena, namely, the shock wave emission and laser-induced bubbles, and their influence on the particle formation have been analyzed. The PLAL method benefits from its robust applicability to produce micro-/nanostructures from nearly all kinds of solid materials; from its potential to eliminate surface contamination without using any chemical precursors or additives; and most importantly, from its ability to produce metastable phase and new structures in a highly non-equilibrium synthetic environment. However, it still suffers from the low productivity associated with high energy consumption; from the generally large size distribution of the products; and from the somewhat "black-box" synthesis environment, namely, the lack of prediction to the products due to the combinatorial interactions. Much effort has been devoted to address these issues, such as studying the time-resolved ablation process using shadowgraph technique, choosing proper liquid, surfactant, and laser parameters; and precisely controlling the ablation process by adjusting the experimental setup. The PLAL method provides a unique approach to investigate the formation of micro-/nanostructures in a highly

reactive and confined environment, and it represents a prolific field for fundamental research and provides prototypes of micro-/nanostructures, nanocomposites, and conjugates for potential applications in sensing, optoelectronics, and biomedicine, etc.

References

[1] R. Nagarajan, T.A. Hatton, Hatton, Nanoparticles: synthesis, stabilization, passivation, and functionalization, in: T.A.H.R. Nagarajan (Ed.), ACS Symposium Series 996, American Chemical Society, Washington, DC, 2008.
[2] H.M. Smith, A.F. Turner, Appl. Opt. 4 (1965) 147.
[3] H.W. Kroto, J.R. Heath, S.C. O'Brien, R.F. Curl, R.E. Smalley, Nature 318 (1985) 162.
[4] A.M. Morales, C.M. Lieber, Science 279 (1998) 208.
[5] D.B. Chrisey, A. Piqué, R.A. McGill, J.S. Horwitz, B.R. Ringeisen, D.M. Bubb, P.K. Wu, Chem. Rev. 103 (2003) 553.
[6] D.B. Chrisey, G.K. Hubler, Pulsed Laser Deposition of Thin Films, John Wiley & Sons, New York, 1994.
[7] P.P. Patil, D.M. Phase, S.A. Kulkarni, S.V. Ghaisas, S.K. Kulkarni, S.M. Kanetkar, S.B. Ogale, V.G. Bhide, Phys. Rev. Lett. 58 (1987) 238.
[8] J. Neddersen, G. Chumanov, T.M. Cotton, Appl. Spectrosc. 47 (1993) 1959.
[9] F. Mafune, J.-y. Kohno, Y. Takeda, T. Kondow, H. Sawabe, J. Phys. Chem. B 104 (2000) 9111.
[10] T. Sasaki, Y. Shimizu, N. Koshizaki, J. Photochem. Photobiol. A 182 (2006) 335.
[11] G.W. Yang, Prog. Mater. Sci. 52 (2007) 648.
[12] G.A. Shafeev, Formation of nanoparticles under laser ablation of solids in liquids, in: S.L. Lombardi (Ed.), Nanoparticles: New Research, Nova Science Publishers, New York, 2008, pp. 1–37.
[13] V. Amendola, M. Meneghetti, Phys. Chem. Chem. Phys. 11 (2009) 3805.
[14] N.G. Semaltianos, Crit. Rev. Solid State Mater. Sci. 35 (2010) 105.
[15] P. Liu, H. Cui, C.X. Wang, G.W. Yang, Phys. Chem. Chem. Phys. 12 (2010) 3942.
[16] T. Asahi, T. Sugiyama, H. Masuhara, Acc. Chem. Res. 41 (2008) 1790.
[17] C.L. Sajti, R. Sattari, B.N. Chichkov, S. Barcikowski, J. Phys. Chem. C 114 (2010) 2421.
[18] T. Tsuji, Y. Tsuboi, N. Kitamura, M. Tsuji, Appl. Surf. Sci. 229 (2004) 365.
[19] T. Tsuji, Y. Okazaki, Y. Tsuboi, M. Tsuji, Jpn. J. Appl. Phys. 46 (2007) 1533.
[20] W. Soliman, N. Takada, K. Sasaki, Appl. Phys. Express 3 (2010) 035201.
[21] A. Menéndez-Manjón, P. Wagener, S. Barcikowski, J. Phys. Chem. C 115 (2011) 5108.
[22] N. Barsch, J. Jakobi, S. Weiler, S. Barcikowski, Nanotechnology 20 (2009) 445603.
[23] Z.J. Yan, R.Q. Bao, D.B. Chrisey, Langmuir 27 (2011) 851.
[24] D. Perez, L.K. Beland, D. Deryng, L.J. Lewis, M. Meunier, Phys. Rev. B 77 (2008) 014108.
[25] Z.J. Yan, R.Q. Bao, Y. Huang, A.N. Caruso, S.B. Qadri, C.Z. Dinu, D.B. Chrisey, J. Phys. Chem. C 114 (2010) 3869.
[26] A. Schwenke, P. Wagener, S. Nolte, S. Barcikowski, Appl. Phys. A 104 (2011) 77.
[27] Y.H. Yeh, M.S. Yeh, Y.P. Lee, C.S. Yeh, Chem. Lett. (1998) 1183.
[28] M.S. Yeh, Y.S. Yang, Y.P. Lee, H.F. Lee, Y.H. Yeh, C.S. Yeh, J. Phys. Chem. B 103 (1999) 6851.
[29] H.Q. Wang, A. Pyatenko, K. Kawaguchi, X. Li, Z. Swiatkowska-Warkocka, N. Koshizaki, Angew. Chem. Int. Ed. 49 (2010) 6361.
[30] X.Y. Li, A. Pyatenko, Y. Shimizu, H.Q. Wang, K. Koga, N. Koshizaki, Langmuir 27 (2011) 5076.
[31] X.Y. Li, J.G. Liu, X.Y. Wang, M. Gao, Z.M. Wang, X.Y. Zeng, Opt. Express 19 (2011) 2846.
[32] M. Kawasaki, J. Phys. Chem. C 115 (2011) 5165.
[33] M. Nath, C.N.R. Rao, R. Popovitz-Biro, A. Albu-Yaron, R. Tenne, Chem. Mater. 16 (2004) 2238.
[34] A. Takami, H. Kurita, S. Koda, J. Phys. Chem. B 103 (1999) 1226.
[35] F. Mafuné, J.-y. Kohno, Y. Takeda, T. Kondow, J. Am. Chem. Soc. 125 (2003) 1686.
[36] F. Mafune, J. Kohno, Y. Takeda, T. Kondow, J. Phys. Chem. B 107 (2003) 12589.
[37] F. Mafune, T. Kondow, Chem. Phys. Lett. 383 (2004) 343.
[38] P.V. Kamat, M. Flumiani, G.V. Hartland, J. Phys. Chem. B 102 (1998) 3123.
[39] D. Werner, A. Furube, T. Okamoto, S. Hashimoto, J. Phys. Chem. C 115 (2011) 8503.
[40] K. Yamada, K. Miyajima, F. Mafuné, J. Phys. Chem. C 111 (2007) 11246.
[41] W.T. Nichols, T. Kodaira, Y. Sasaki, Y. Shimizu, T. Sasaki, N. Koshizaki, J. Phys. Chem. B 110 (2005) 83.
[42] Y.B. Zel'dovich, Y.P. Raizer, Physics of Shock Waves and High-Temperature Hydrodynamic Phenomena, Academic Press, New York, 1966–1967.
[43] T.E. Itina, J. Phys. Chem. C 115 (2010) 5044.
[44] R. Petkovsek, P. Gregorcic, J. Appl. Phys. 102 (2007) 044909.
[45] Y. Tomita, M. Tsubota, N. An-Naka, J. Appl. Phys. 93 (2003) 3039.
[46] O. Yavas, P. Leiderer, H.K. Park, C.P. Grigoropoulos, C.C. Poon, A.C. Tam, Phys. Rev. Lett. 72 (1994) 2021.
[47] P. Lorazo, L.J. Lewis, M. Meunier, Phys. Rev. B 73 (2006) 134108.
[48] V. Kostrykin, M. Niessen, J. Jandeleit, W. Schulz, E.-W. Kreutz, R. Poprawe, Proc. SPIE 3343 (1998) 971.
[49] N.M. Bulgakova, A.V. Bulgakov, Appl. Phys. A 73 (2001) 199.
[50] D. von der Linde, K. Sokolowski-Tinten, J. Bialkowski, Appl. Surf. Sci. 109–110 (1997) 1.

[51] A. Miotello, R. Kelly, Appl. Phys. A 69 (1999) S67.
[52] V.P. Carey, Liquid Vapor Phase Change Phenomena an Introduction to the Thermophysics of Vaporization and Condensation Processes in Heat Transfer Equipment, second ed., Taylor & Francis, New York, 2008.
[53] A. Miotello, R. Kelly, Appl. Phys. Lett. 67 (1995) 3535.
[54] K.H. Song, X. Xu, Appl. Surf. Sci. 127–129 (1998) 111.
[55] P. Lorazo, L.J. Lewis, M. Meunier, Phys. Rev. Lett. 91 (2003) 225502.
[56] D. Perez, L.J. Lewis, Phys. Rev. B 67 (2003) 184102.
[57] K.Y. Niu, J. Yang, S.A. Kulinich, J. Sun, H. Li, X.W. Du, J. Am. Chem. Soc. 132 (2010) 9814.
[58] M.A. Sobhan, M.J. Withford, E.M. Goldys, Langmuir 26 (2010) 3156.
[59] Z. Zhang, G. Gogos, Phys. Rev. B 69 (2004) 235403.
[60] B. Toftmann, J. Schou, J.G. Lunney, Phys. Rev. B 67 (2003) 104101.
[61] B.X. Wu, Y.C. Shin, J. Appl. Phys. 99 (2006) 084310.
[62] C.D. Ohl, O. Lindau, W. Lauterborn, Phys. Rev. Lett. 80 (1998) 393.
[63] H.-C. Chu, S. Vo, G.A. Williams, Phys. Rev. Lett. 102 (2009) 204301.
[64] S.I. Kudryashov, V.D. Zvorykin, Phys. Rev. E 78 (2008) 036404.
[65] O. Yavas, P. Leiderer, H.K. Park, C.P. Grigoropoulos, C.C. Poon, W.P. Leung, N. Do, A.C. Tam, Phys. Rev. Lett. 70 (1993) 1830.
[66] Z.J. Yan, R.Q. Bao, Y. Huang, D.B. Chrisey, J. Phys. Chem. C 114 (2010) 11370.
[67] M.S. Plesset, A. Prosperetti, Annu. Rev. Fluid Mech. 9 (1977) 145.
[68] K. Sasaki, N. Takada, Pure Appl. Chem. 82 (2010) 1317.
[69] N. Takada, T. Nakano, K. Sasaki, Appl. Phys. A 101 (2010) 255.
[70] W. Soliman, N. Nakano, N. Takada, K. Sasaki, Jpn. J. Appl. Phys. 49 (2010).
[71] J.H. Bang, K.S. Suslick, Adv. Mater. 22 (2010) 1039.
[72] C.E. Brennen, Cavitation and Bubble Dynamics, Oxford University Press, Oxford, 1995.
[73] P.T.H.M. Verhallen, L.J.P. Oomen, A.J.J.M.v.d. Elsen, J. Kruger, J.M.H. Fortuin, Chem. Eng. Sci. 39 (1984) 1535.
[74] W. Lauterborn, T. Kurz, R. Mettin, C.D. Ohl, Experimental and theoretical bubble dynamics, Adv. Chem. Phys. 110 (1999) 295–380.
[75] X.-M. Liu, et al., Chin. Phys. B 17 (2008) 2574.
[76] B.P. Binks, Curr. Opin. Colloid Interface Sci. 7 (2002) 21.
[77] T.S. Horozov, Curr. Opin. Colloid Interface Sci. 13 (2008) 134.
[78] M.S. Tillack, D.W. Blair, S.S. Harilal, Nanotechnology 15 (2004) 390.
[79] B.S. Luk'yanchuk, W. Marine, S.I. Anisimov, Laser Phys. 8 (1998) 291.
[80] S. Senadheera, B. Tan, K. Venkatakrishnan, J. Nanotechnol. 2009 (2009) 590763.
[81] S.I. Anisimov, B.S. Luk'yanchuk, Physics-Uspekhi 45 (2002) 293.
[82] Y. Nakata, J. Muramoto, T. Okada, M. Maeda, J. Appl. Phys. 91 (2002) 1640.
[83] J. Muramoto, T. Inmaru, Y. Nakata, T. Okada, M. Maeda, Appl. Phys. Lett. 77 (2000) 2334.
[84] D.B. Geohegan, A.A. Puretzky, G. Duscher, S.J. Pennycook, Appl. Phys. Lett. 72 (1998) 2987.
[85] C.X. Wang, P. Liu, H. Cui, G.W. Yang, Appl. Phys. Lett. 87 (2005) 201913.
[86] A.V. Gusarov, A.G. Gnedovets, I. Smurov, J. Appl. Phys. 88 (2000) 4352.
[87] H.B. Zeng, W.P. Cai, Y. Li, J.L. Hu, P.S. Liu, J. Phys. Chem. B 109 (2005) 18260.
[88] C.H. Liang, Y. Shimizu, M. Masuda, T. Sasaki, N. Koshizaki, Chem. Mater. 16 (2004) 963.
[89] Z.J. Yan, G. Compagnini, D.B. Chrisey, J. Phys. Chem. C 115 (2011) 5058.
[90] J.-P. Sylvestre, S. Poulin, A.V. Kabashin, E. Sacher, M. Meunier, J.H.T. Luong, J. Phys. Chem. B 108 (2004) 16864.
[91] H. Muto, K. Yamada, K. Miyajima, F. Mafuné, J. Phys. Chem. C 111 (2007) 17221.
[92] W.T. Nichols, T. Sasaki, N. Koshizaki, J. Appl. Phys. 100 (2006) 114913.
[93] D.C. Schinca, et al., J. Phys. D: Appl. Phys. 42 (2009) 215102.
[94] S. Barcikowski, F. Mafuneǐ, J. Phys. Chem. C 115 (2011) 4985.
[95] E. Messina, E. Cavallaro, A. Cacciola, M.A. Iatì, P.G. Gucciardi, F. Borghese, P. Denti, R. Saija, G. Compagnini, M. Meneghetti, V. Amendola, O.M. Maragò, ACS Nano 5 (2011) 905.
[96] P. Liu, Y. Liang, X.Z. Lin, C.X. Wang, G.W. Yang, ACS Nano 5 (2011) 4748.
[97] A.V. Simakin, V.V. Voronov, G.A. Shafeev, R. Brayner, F. Bozon-Verduraz, Chem. Phys. Lett. 348 (2001) 182.
[98] S.I. Dolgaev, A.V. Simakin, V.V. Voronov, G.A. Shafeev, F. Bozon-Verduraz, Appl. Surf. Sci. 186 (2002) 546.
[99] D. Werner, S. Hashimoto, T. Tomita, S. Matsuo, Y. Makita, J. Phys. Chem. C 112 (2008) 1321.
[100] F. Mafune, J. Kohno, Y. Takeda, T. Kondow, H. Sawabe, J. Phys. Chem. B 104 (2000) 8333.
[101] M. Prochazka, J. Stepanek, B. Vlckova, I. Srnova, P. Maly, J. Mol. Struct. 410 (1997) 213.
[102] I. Srnova, M. Prochazka, B. Vlckova, J. Stepanek, P. Maly, Langmuir 14 (1998) 4666.
[103] M. Prochazka, P. Mojzes, J. Stepanek, B. Vlckova, P.Y. Turpin, Anal. Chem. 69 (1997) 5103.
[104] C.H. Bae, S.H. Nam, S.M. Park, Appl. Surf. Sci. 197 (2002) 628.
[105] C. He, T. Sasaki, Y. Zhou, Y. Shimizu, M. Masuda, N. Koshizaki, Adv. Funct. Mater. 17 (2007) 3554.
[106] T. Tsuji, D.H. Thang, Y. Okazaki, M. Nakanishi, Y. Tsuboi, M. Tsuji, Appl. Surf. Sci. 254 (2008) 5224.
[107] H. Aleali, L. Sarkhosh, R. Karimzadeh, N. Mansour, Phys. Status Solidi B 248 (2011) 680.
[108] F. Bian, Y.C. Tian, R. Wang, H.X. Yang, H.X. Xu, S. Meng, J.M. Zhao, Nano Lett. 11 (2011) 3251.
[109] F. Mafune, J. Kohno, Y. Takeda, T. Kondow, H. Sawabe, J. Phys. Chem. B 105 (2001) 5114.
[110] F. Mafune, J. Kohno, Y. Takeda, T. Kondow, J. Phys. Chem. B 105 (2001) 9050.
[111] F. Mafune, J.Y. Kohno, Y. Takeda, T. Kondow, J. Phys. Chem. B 106 (2002) 7575.
[112] H. Muto, K. Miyajima, F. Mafune, J. Phys. Chem. C 112 (2008) 5810.
[113] A.V. Kabashin, M. Meunier, J. Appl. Phys. 94 (2003) 7941.
[114] A.V. Kabashin, M. Meunier, C. Kingston, J.H.T. Luong, J. Phys. Chem. B 107 (2003) 4527.
[115] J.P. Sylvestre, A.V. Kabashin, E. Sacher, M. Meunier, J.H.T. Luong, J. Am. Chem. Soc. 126 (2004) 7176.
[116] K. Saitow, T. Yamamura, T. Minami, J. Phys. Chem. C 112 (2008) 18340.
[117] S. Petersen, A. Barchanski, U. Taylor, S. Klein, D. Rath, S. Barcikowski, J. Phys. Chem. C 115 (2011) 5152.
[118] F. Mafune, J.Y. Kohno, Y. Takeda, T. Kondow, J. Phys. Chem. B 107 (2003) 4218.
[119] W.T. Nichols, T. Sasaki, N. Koshizaki, J. Appl. Phys. 100 (2006) 114911.
[120] W.T. Nichols, T. Sasaki, N. Koshizaki, J. Appl. Phys. 100 (2006) 114912.
[121] Z.J. Yan, R.Q. Bao, D.B. Chrisey, Nanotechnology 21 (2010) 145609.
[122] H. Usui, T. Sasaki, N. Koshizaki, Appl. Phys. Lett. 87 (2005) 063105.
[123] H. Usui, Y. Shimizu, T. Sasaki, N. Koshizaki, J. Phys. Chem. B 109 (2005) 120.
[124] Z.J. Yan, R.Q. Bao, D.B. Chrisey, Chem. Phys. Lett. 497 (2010) 205.
[125] L. Yang, P.W. May, L. Yin, T.B. Scott, Nanotechnology 18 (2007) 215602.
[126] H.B. Zeng, W.P. Cai, J.L. Hu, G.T. Duan, P.S. Liu, Y. Li, Appl. Phys. Lett. 88 (2006) 171910.
[127] H. Zeng, Z. Li, W. Cai, B. Cao, P. Liu, S. Yang, J. Phys. Chem. B 111 (2007) 14311.
[128] H.B. Zeng, P.S. Liu, W.P. Cai, X.L. Cao, S.K. Yang, Cryst. Growth Des. 7 (2007) 1092.
[129] Y. Ishikawa, Y. Shimizu, T. Sasaki, N. Koshizaki, J. Colloid Interface Sci. 300 (2006) 612.
[130] C. He, T. Sasaki, Y. Shimizu, N. Koshizaki, Appl. Surf. Sci. 254 (2008) 2196.
[131] P. Wagener, A. Schwenke, B.N. Chichkov, S. Barcikowski, J. Phys. Chem. C 114 (2010) 7618.
[132] Q.A. Drmosh, M.A. Gondal, Z.H. Yamani, T.A. Saleh, Appl. Surf. Sci. 256 (2010) 4661.
[133] Z.J. Yan, R.Q. Bao, R.N. Wright, D.B. Chrisey, Appl. Phys. Lett. 97 (2010) 124106.
[134] K.Y. Niu, J. Yang, S.A. Kulinich, J. Sun, X.W. Du, Langmuir 26 (2010) 16652.
[135] C.H. Liang, Y. Shimizu, T. Sasaki, N. Koshizaki, J. Mater. Res. 19 (2004) 1551.
[136] C.H. Liang, Y. Shimizu, T. Sasaki, N. Koshizaki, Appl. Phys. A 80 (2005) 819.
[137] A.S. Nikolov, P.A. Atanasov, D.R. Milev, T.R. Stoyanchov, A.D. Deleva, Z.Y. Peshev, Appl. Surf. Sci. 255 (2009) 5351.
[138] P.S. Liu, W.P. Cai, M. Fang, Z.G. Li, H.B. Zeng, J.L. Hu, X.D. Luo, W.P. Jing, Nanotechnology 20 (2009) 285707.
[139] O.R. Musaev, A.E. Midgley, J.M. Wrobel, J. Yan, M.B. Kruger, J. Appl. Phys. 106 (2009) 054306.
[140] A. Baladi, R.S. Mamoory, Appl. Surf. Sci. 256 (2010) 7559.
[141] E. Stratakis, M. Barberoglou, C. Fotakis, G. Viau, C. Garcia, G.A. Shafeev, Opt. Express 17 (2009) 12650.
[142] B. Kumar, R.K. Thareja, J. Appl. Phys. 108 (2010) 064906.
[143] I.L. Liu, P. Shen, S.Y. Chen, J. Phys. Chem. C 114 (2010) 7751.
[144] C.A. Crouse, E. Shin, P.T. Murray, J.E. Spowart, Mater. Lett. 64 (2010) 271.
[145] C.H. Liang, T. Sasaki, Y. Shimizu, N. Koshizaki, Chem. Phys. Lett. 389 (2004) 58.
[146] T.X. Phuoc, B.H. Howard, D.V. Martello, Y. Soong, M.K. Chyu, Opt. Lasers Eng. 46 (2008) 829.
[147] Z.J. Yan, R.Q. Bao, C.M. Busta, D.B. Chrisey, Nanotechnology 22 (2011) 265610.
[148] X.Z. Lin, P. Liu, J.M. Yu, G.W. Yang, J. Phys. Chem. C 113 (2009) 17543.
[149] A. Nath, A. Khare, J. Appl. Phys. 110 (2011) 043111.
[150] M. Muniz-Miranda, C. Gellini, E. Giorgetti, J. Phys. Chem. C 115 (2011) 5021.
[151] P.S. Liu, W.P. Cai, H.B. Zeng, J. Phys. Chem. C 112 (2008) 3261.
[152] V. Amendola, P. Riello, M. Meneghetti, J. Phys. Chem. C 115 (2011) 5140.
[153] J. Zhang, C.Q. Lan, Mater. Lett. 62 (2008) 1521.
[154] H.M. Zhang, C.H. Liang, Z.F. Tian, G.Z. Wang, W.P. Cai, J. Phys. Chem. C 114 (2010) 12524.
[155] M.S.F. Lima, F.P. Ladario, R. Riva, Appl. Surf. Sci. 252 (2006) 4420.
[156] F.B.F. Barreca, N. Acacia, S. Spadaro, G. Curro, F. Neri, Mater. Chem. Phys. 127 (2011) 197.
[157] C.H. Liang, Y. Shimizu, T. Sasaki, N. Koshizaki, J. Phys. Chem. B 107 (2003) 9220.
[158] Y. Guo-Wei, et al., J. Phys.: Condens. Matter 10 (1998) 7923.
[159] J.B. Wang, C.Y. Zhang, X.L. Zhong, G.W. Yang, Chem. Phys. Lett. 361 (2002) 86.
[160] L. Yang, P.W. May, L. Yin, J.A. Smith, K.N. Rosser, J. Nanopart. Res. 9 (2007) 1181.
[161] A. Santagata, A. De Bonis, A. De Giacomo, M. Dell'Aglio, A. Laurita, G.S. Senesi, R. Gaudiuso, S. Orlando, R. Teghil, G.P. Parisi, J. Phys. Chem. C 115 (2011) 5160.
[162] P. Liu, Y.L. Cao, C.X. Wang, X.Y. Chen, G.W. Yang, Nano Lett. 8 (2008) 2570.
[163] T. Sugiyama, S.-i. Ryo, I. Oh, T. Asahi, H. Masuhara, J. Photochem. Photobiol. A 207 (2009) 7.
[164] V. Svrcek, T. Sasaki, Y., Shimizu, N. Koshizaki, Appl. Phys. Lett. 89 (2006).
[165] P.G. Kuzmin, G.A. Shafeev, V.V. Bukin, S.V. Garnov, C. Farcau, R. Carles, B. Warot-Fonrose, V. Guieu, G. Viau, J. Phys. Chem. C 114 (2010) 15266.
[166] S. Yang, W. Cai, G. Liu, H. Zeng, P. Liu, J. Phys. Chem. C 113 (2009) 6480.
[167] S.K. Yang, W.P. Cai, H.W. Zhang, X.X. Xu, H.B. Zeng, J. Phys. Chem. C 113 (2009) 19091.
[168] E. Jimenez, K. Abderrafi, R. Abargues, J.L. Valdes, J.P. Martinez-Pastor, Langmuir 26 (2010) 7458.
[169] K. Abderrafi, R.G. Calzada, M.B. Gongalsky, I. Suarez, R. Abarques, V.S. Chirvony, V.Y. Timoshenko, R. Ibanez, J.P. Martinez-Pastor, J. Phys. Chem. C 115 (2011) 5147.
[170] P. Liu, C.X. Wang, X.Y. Chen, G.W. Yang, J. Phys. Chem. C 112 (2008) 13450.
[171] P. Liu, Y.L. Cao, X.Y. Chen, G.W. Yang, Cryst. Growth Des. 9 (2009) 1390.

[172] J. Jakobi, S. Petersen, A. Meneĭndez-Manjoĭn, P. Wagener, S. Barcikowski, Langmuir 26 (2010) 6892.
[173] I. Lee, S.W. Han, K. Kim, Chem. Commun. (2001) 1782.
[174] H. Han, Y. Fang, Z. Li, H. Xu, Appl. Phys. Lett. 92 (2008) 023116.
[175] X.X. Huang, W.G. Zhang, Appl. Surf. Sci. 254 (2008) 3403.
[176] W.W. Gong, Z.H. Zheng, J.J. Zheng, W. Gao, X.B. Hu, X.G. Ren, J. Phys. Chem. C 112 (2008) 9983.
[177] S.W. Mhin, J.H. Ryu, K.M. Kim, G.S. Park, H.W. Ryu, K.B. Shim, T. Sasaki, N. Koshizaki, Appl. Phys. A 96 (2009) 435.
[178] G. Ledoux, D. Amans, C. Dujardin, K. Masenelli-Varlot, Nanotechnology 20 (2009) 445605.
[179] D. Amans, C. Malaterre, M. Diouf, C. Mancini, F. Chaput, G. Ledoux, G. Breton, Y. Guillin, C. Dujardin, K. Masenelli-Varlot, P. Perriat, J. Phys. Chem. C 115 (2011) 5131.
[180] S.W. Mhin, J.H. Ryu, K.M. Kim, G.S. Park, H.W. Ryu, K.B. Shim, T. Sasaki, N. Koshizaki, Nanoscale Res. Lett. 4 (2009) 888.
[181] T. Sugiyama, T. Asahi, H. Masuhara, Chem. Lett. 33 (2004) 724.
[182] R. Yasukuni, M. Sliwa, J. Hofkens, F.C. De Schryver, A. Herrmann, K. Mullen, T. Asahi, Jpn. J. Appl. Phys. 48 (2009) 065002.
[183] X.W. Lou, L.A. Archer, Z. Yang, Adv. Mater. 20 (2008) 3987.
[184] Z.J. Yan, Q. Zhao, D.B. Chrisey, Mater. Chem. Phys. 130 (2011) 403.
[185] C. Dong, Z.J., Yan, J., Kokx, D.B., Chrisey, C.Z., Dinu, Appl. Surf Sci., http://dx.doi.org/10.1016/j.apsusc.2011.07.076.
[186] Z.J. Yan, R.Q. Bao, C.Z. Dinu, Y. Huang, A.N. Caruso, D.B. Chrisey, J. Optoelectron. Adv. Mater. 12 (2010) 437.
[187] K.N. Jha, G.R. Freeman, Can. J. Chem. 51 (1973) 2033.
[188] G. Gilarowski, W. Erley, H. Ibach, Surf. Sci. 351 (1996) 156.

[189] A.V. Kabashin, P. Delaporte, A. Pereira, D. Grojo, R. Torres, T. Sarnet, M. Sentis, Nanoscale Res. Lett. 5 (2010) 454.
[190] S.K. Yang, H.B. Zeng, H.P. Zhao, H.W. Zhang, W.P. Cai, J. Mater. Chem. 21 (2011) 4432.
[191] S. Yang, W. Cai, H. Zhang, H. Zeng, Y. Lei, J. Phys. Chem. C 115 (2011) 7279.
[192] I. Uzcanga, I. Bezverkhyy, P. Afanasiev, C. Scott, M. Vrinat, Chem. Mater. 17 (2005) 3575.
[193] D.G. Shchukin, H. Mohwald, Phys. Chem. Chem. Phys. 8 (2006) 3496.
[194] A.D. Smigelskas, E.O. Kirkendall, Trans. AIME 171 (1947) 130.
[195] Y.D. Yin, R.M. Rioux, C.K. Erdonmez, S. Hughes, G.A. Somorjai, A.P. Alivisatos, Science 304 (2004) 711.
[196] H.J. Fan, M. Knez, R. Scholz, D. Hesse, K. Nielsch, M. Zacharias, U. Gosele, Nano Lett. 7 (2007) 993.
[197] R. Nakamura, D. Tokozakura, H. Nakajima, J.-G. Lee, H. Mori, J. Appl. Phys 101 (2007) 074303.
[198] S. Yang, W. Cai, J. Yang, H. Zeng, Langmuir 25 (2009) 8287.
[199] G. Viau, V. Collière, L.M. Lacroix, G.A. Shafeev, Chem. Phys. Lett. 501 (2011) 419.
[200] H. He, W.P. Cai, Y.X. Lin, B.S. Chen, Chem. Commun. 46 (2010) 7223.
[201] C.J. Murphy, Science 298 (2002) 2139.
[202] L. Rossi, S. Sacanna, W.T.M. Irvine, P.M. Chaikin, D.J. Pine, A.P. Philipse, Soft Matter 7 (2011) 4139.
[203] L. Yang, P.W. May, L. Yin, R. Brown, T.B. Scott, Chem. Mater. 18 (2006) 5058.
[204] L. Yang, P.W. May, Y. Huang, L. Yin, J. Mater. Chem. 17 (2007) 1255.
[205] L.C. Nistor, G. Epurescu, M. Dinescu, G. Dinescu, IOP Conf. Ser.: Mater. Sci. Eng. 15 (2010) 012067.
[206] S.C. Singh, R. Gopal, J. Phys. Chem. C 114 (2010) 9277.